



University of Pennsylvania
ScholarlyCommons

Publicly Accessible Penn Dissertations


2019

Polymer Infiltration Under Extreme Confinement

David Ring

University of Pennsylvania, david.j.ring@outlook.com

Follow this and additional works at: <https://repository.upenn.edu/edissertations>

 Part of the [Chemical Engineering Commons](#), and the [Condensed Matter Physics Commons](#)

Recommended Citation

Ring, David, "Polymer Infiltration Under Extreme Confinement" (2019). *Publicly Accessible Penn Dissertations*. 3484.

<https://repository.upenn.edu/edissertations/3484>

This paper is posted at ScholarlyCommons. <https://repository.upenn.edu/edissertations/3484>
For more information, please contact repository@pobox.upenn.edu.

Polymer Infiltration Under Extreme Confinement

Abstract

Polymer nanocomposites with high nanoparticle loadings are ubiquitous in nature but difficult to replicate synthetically. A simple technique to create such polymer nanocomposites is to form a bi-layer of a nanoparticle thin film atop a polymer thin film and anneal above the polymer glass transition temperature to induce wicking. This Capillary Rise Infiltration (CaRI) of polymers into nanoparticle thin films is a promising method to create interesting biomimetic composites with enhanced material properties, but also raises important theoretical questions about confinement, capillarity, and polymer dynamics. Therefore, I use molecular dynamics simulations (MD) and continuum theory to understand the impact of confinement on infiltrating polymers. In Chapter 2, I observe that polymers will form porous nanocomposites when there is not enough polymer to fill the voids in the nanoparticle packings. These undersaturated CaRI systems (UCaRI) can be used to form graded or uniform porous composites if the bi-layer is annealed for short or long times, respectively. Due to polymer bridges formed during annealing, these porous nanocomposites have markedly enhanced mechanical properties even when the fraction of polymer is very low. Chapter 3 investigates the effect of confinement on critical contact angle above which infiltration halts. It is determined that the confinement of polymers in the melt does not significantly affect the critical contact angle, which remains independent of the chain length for sufficiently long chains, but depends strongly on the chain stiffness. Finally, Chapter 4 investigates the effect of varying cross-section on the free energy landscape of infiltrating polymers. I discover that barriers can be introduced into the infiltration free energy as a result of the large change in free surface area between constrictions and expansions along the length of the capillary. This leads to polymer infiltration that occurs stepwise from minimum to minimum, like an activated process. Thus, free energy due to wetting and confinement in nanopores has a significant impact on the infiltration behavior of polymers and the formation polymer nanocomposites.

Degree Type

Dissertation

Degree Name

Doctor of Philosophy (PhD)

Graduate Group

Chemical and Biomolecular Engineering

First Advisor

Daeyeon Lee

Second Advisor

Robert A. Riggleman

Keywords

capillary, confinement, infiltration, molecular dynamics, nanoparticles, polymer

Subject Categories

Chemical Engineering | Condensed Matter Physics

POLYMER INFILTRATION UNDER EXTREME CONFINEMENT

David J. Ring

A DISSERTATION

in

Chemical & Biomolecular Engineering

Presented to the Faculties of the University of Pennsylvania

in

Partial Fulfillment of the Requirements for the

Degree of Doctor of Philosophy

2019

Supervisor of Dissertation

Daeyeon Lee

Professor of Chemical and Biomolecular Engineering (CBE)

Co-Supervisor of Dissertation

Robert A. Riggleman

Associate Professor of CBE

Graduate Group Chairperson

John C. Crocker, Professor of Chemical and Biomolecular Engineering

Dissertation Committee

Zahra Fakhraai, Associate Professor of Chemistry and CBE

Ravi Radhakrishnan, Professor of Bioengineering and CBE

To my family

ACKNOWLEDGMENTS

I would first like to acknowledge my advisors, Robert Riggleman and Daeyeon Lee for their support throughout my thesis. You were always patient and helpful when I struggled and encouraging when I succeeded. I will always admire your dedication to research and ability to bring out the best in people. I want to thank Daeyeon for being quick to provide feedback whenever I was preparing a presentation, report, or paper. I also want to thank Rob for always being willing to meet and help me improve my simulations, ideas, and presentations.

To my friend and collaborator, Jyo Lyn Hor, I am grateful for the time we spent together the last 5 years. I enjoyed sitting next to you in the lab, our daily tea breaks, and our Kombucha brewing side project. I'm very happy to have published a paper with you.

I am forever grateful to Emily Lin from Rob Riggleman's group for being a good friend, helpful coworker, and lunch buddy. I always enjoy our discussions of research, dating, and life over lunch and hope that we can have many more.

To all the members of the Lee and Riggleman labs who I have not mentioned by name, I would like to say that you were all fantastic. I especially appreciate how the Lee lab responded positively to my work in group meetings even though my simulations were so different from what everyone else was doing. I will also miss the lab cleanup and hope that someone else will take over meticulously cleaning the balance.

A special thanks to my family who supported me from afar. Mom and Dad, I'm grateful for your constant love and support during the many ups and downs of my time in

Philadelphia. To my sisters and sister-in-law, thank you for always encouraging me in my work by listening even when I threw around jargon and rambled on for far too long. To my twin brother, thank you for the time spent canoeing and talking about computers. To my nephew and niece, thank you for staring delightedly at visualizations of my polymer simulations. I hope that one day you pursue an advanced degree too.

Finally, I would like to thank my boyfriend for the support and encouragement he's shown me over the last 3 years. You've shown me that there's more to life than just work and achievement.

ABSTRACT

POLYMER INFILTRATION UNDER EXTREME CONFINEMENT

David J. Ring

Daeyeon Lee and Robert A. Riggleman

Polymer nanocomposites with high nanoparticle loadings are ubiquitous in nature but difficult to replicate synthetically. A simple technique to create such polymer nanocomposites is to form a bi-layer of a nanoparticle thin film atop a polymer thin film and anneal above the polymer glass transition temperature to induce wicking. This Capillary Rise Infiltration (CaRI) of polymers into nanoparticle thin films is a promising method to create interesting biomimetic composites with enhanced material properties, but also raises important theoretical questions about confinement, capillarity, and polymer dynamics. Therefore, I use molecular dynamics simulations (MD) and continuum theory to understand the impact of confinement on infiltrating polymers. In Chapter 2, I observe that polymers will form porous nanocomposites when there is not enough polymer to fill the voids in the nanoparticle packings. These undersaturated CaRI systems (UCaRI) can be used to form graded or uniform porous composites if the bi-layer is annealed for short or long times, respectively. Due to polymer bridges formed during annealing, these porous nanocomposites have markedly enhanced mechanical properties even when the fraction of polymer is very low. Chapter 3 investigates the effect of confinement on critical contact angle above which infiltration halts. It is determined that the confinement of polymers in the melt does not significantly affect the critical contact angle, which remains independent of the chain length for sufficiently long chains, but depends strongly on the chain stiffness. Finally, Chapter 4 investigates the effect of

varying cross-section on the free energy landscape of infiltrating polymers. I discover that barriers can be introduced into the infiltration free energy as a result of the large change in free surface area between constrictions and expansions along the length of the capillary. This leads to polymer infiltration that occurs stepwise from minimum to minimum, like an activated process. Thus, free energy due to wetting and confinement in nanopores has a significant impact on the infiltration behavior of polymers and the formation polymer nanocomposites.

TABLE OF CONTENTS

ACKNOWLEDGMENTS	III
ABSTRACT.....	V
LIST OF TABLES	IX
LIST OF ILLUSTRATIONS.....	X
CHAPTER 1: INTRODUCTION.....	1
1.1 Nanocomposites with high filler fractions and their fabrication techniques.....	1
1.2 Capillary Rise Infiltration (CaRI)	4
1.3 Capillarity-induced Polymer Infiltration in Nanoscale Pores (< 100 nm).....	5
1.4 Free Energy in confinement	9
1.5 Unresolved topics in capillary rise of polymer in nanoscale pores.....	10
1.6 Outline of this thesis.....	12
CHAPTER 2: MOLECULAR DYNAMICS SIMULATIONS OF UNDERSATURATED CAPILLARY RISE INFILTRATION IN NANOPARTICLE PACKINGS	13
2.1 Introduction.....	13
2.2 Model Parameters and Methods	16
2.3 Infiltrating Films and Analyzing Polymer Distribution.....	18
2.4 Infiltration dynamics and surface spreading	21
2.5 Summary.....	25
CHAPTER 3: CRITICAL CONTACT ANGLE TO INDUCE CAPILLARY RISE OF POLYMERS IN NANOPORES DOES NOT DEPEND ON CHAIN LENGTH	26
3.1 Introduction.....	26
3.2 Model details and system setup.....	28
3.3 Correlating contact angle with interatomic interactions	34

3.4	Computing Critical Contact Angle from Dynamics	36
3.5	Computing Critical Contact Angle using Umbrella Sampling	38
3.6	Deriving the Free Energy Model.....	41
3.7	Critical contact angle of polymer infiltration into nanoparticle packings	43
3.8	Summary.....	47
 CHAPTER 4: INFILTRATION OF POLYMER INTO NANO-CAPILLARIES WITH PERIODICALLY VARYING CROSS-SECTION		48
4.1	Introduction.....	48
4.2	Making Wavy Capillaries.....	50
4.3	Derivation of the Free Energy Model	51
4.4	INDirect Umbrella Sampling	54
4.5	Infiltration Comparison.....	57
4.6	Summary.....	59
 CHAPTER 5: CONCLUSIONS AND OUTLOOK		60
5.1	Conclusions	60
5.2	Confinement Free Energy of Stiff Polymers	62
5.3	Free Energy landscape with solvent addition	63
5.4	Free energy of infiltration in packings of anisotropic particles	66
5.5	Influence of dynamics and extensional viscosity.....	68
 BIBLIOGRAPHY		71

LIST OF TABLES

Table 2.1: Quantities used in the calculation of the imbibition coefficient.....	24
Table 3.1: Measures of chain stiffness for fully flexible and semi-flexible chains	29
Table 3.2: LJ Parameters for infiltration.....	31

LIST OF ILLUSTRATIONS

Figure 1.1: (a) – (b) Abalone nacre has a brick-and-mortar microstructure composed of brittle calcium carbonate glued together with small amounts of chitin. This structure has enhanced hardness and fracture toughness, two properties which are hard to achieve concurrently. (c) – (e) The dactyl club of the mantis shrimp has a helicoidal closed packed group of chitin fibers reinforced by mineralization as shown in the diagram and SEM micrograph. This structure provides excellent energy dissipation upon impact[9].2

Figure 1.2: (a) The ratio of penetrant permeability in the nanocomposite to that in the pure polymer as a function of filler volume fraction. Filler volume fraction is estimated from $\phi_f = m_f / (m_f + m_p \rho_f / \rho_p)$, where m and ρ refer to the mass and density, respectively, of filler (f) and polymer (p) used in the nanocomposite. The dashed line represents the Maxwell model prediction[3]. Our data (open circles) are for methane permeation at 25°C in PMP containing nanoscale fumed silica (TS-530 from Cabot). Included for comparison are the data of Barrer et al. [14] for propane permeation at 40°C in natural rubber containing ZnO filler (solid circles). (b) The effect of fumed silica (TS-530) content on n-butane permeability and n-butane/methane selectivity of glassy PMP. These data were acquired at 25°C from mixtures composed of 98 mole % methane and 2 mole % n-butane at a feed pressure of 11.2 atm and a permeate pressure of 1 atm. [3]3

Figure 1.3: (a & b) Schematic and SEM micrographs of Capillary Rise Infiltration (CaRI) of polymers into nanoparticle packings. The process starts with a bi-layer

thin film of nanoparticles and polymers that is then annealed above T_g of the polymers to induce wicking and form a composite layer (c) Infiltration dynamics of the polymers rising through the nanoparticle packing exhibit height vs time scaling consistent with the Lucas-Wasburn Equation[4].....5

Figure 1.4: Real and Ideal chains under cylindrical confinement[38].....10

Figure 2.1: Refractive index of the film as a function of distance from the substrate at various annealing intervals, with the schematic illustration representing the film morphology at each stage. The bilayer film composed of a 190 nm TiO_2 NP layer ($n_{NP} = 1.67$) on a 45 nm PS layer ($n_{PS} = 1.58$) is annealed at $150^\circ C$ [20].14

Figure 2.2: Mechanical properties of the nanoporous PINFs measured using nanoindentation tests. (a) The normalized hardness and (b) the normalized modulus of the composite increase with the PS volume fraction (ϕ_{PS}). Every data point is expressed as a statistical average of nine partial loading cycles with loads 40–500 μN at 49 random spots on the sample, with indent depths of 100–200 nm. The error bar represents the standard deviation of the mean. The TiO_2 NP film’s hardness and reduced modulus are 271.6 ± 21.4 MPa and 12.9 ± 0.5 GPa, respectively, whereas the PS film’s hardness and modulus are 292.2 ± 28.9 MPa and 6.9 ± 0.3 GPa, respectively[20].....15

Figure 2.3: (a) Polymer/NP bilayer film prior to annealing (left) and the PINF after annealing (right). (b) The local polymer density profile along the z-axis with annealing time shows that the polymer infiltrates and gradually distributes throughout the NP packing to form a uniform PINF. (c) Probability that a

bead on the surface of the NPs is not in contact with a polymer monomer as a function of time. The bottom 30σ is closest to the polymer film, and the rapid decrease in the probability indicates that this layer of NPs quickly becomes covered with polymer, and the UCARI film gradually homogenizes with equilibration. Homogenization is accelerated by increasing the temperature from 0.7 to 1.0 around $4 \times 10^5 t/\tau_{LJ}$19

Figure 2.4: The probability that a polymer chain is in contact with two nanoparticles (P_{bridging}) for three different polymer fractions ($\phi_{\text{poly}} = 0.013, 0.03$ and 0.13). P_{bridging} increases drastically with lower ϕ_{poly} , suggesting the accumulation of polymer chains near particle contacts. Visualizations of each trajectory show that in lower fraction PINFs, the polymers form rings around nanoparticle-nanoparticle contacts.21

Figure 2.5: The height squared of the composite layer for the 85% and 99% cut-offs showing various linear regions with changing slopes, indicative of a transition in infiltration mechanism as (1) polymer infiltrates via capillary rise consistent with the Lucas-Washburn model, (2) polymer layer is depleted and polymer spreads via a slower surface diffusion behavior, (3) polymer has distributed throughout the packing and the trajectory stops evolving. (4) end of trajectory showing that infiltration has stopped (annealed at $T = 1$). The inset shows $\rho(z)$ at the end of the trajectory to demonstrate that the polymer has spread throughout the entire nanoparticle packing uniformly.22

Figure 2.6: Mean squared displacement of polymers with 10 chain repeat units.....23

Figure 3.1: The bond autocorrelation function decays exponentially with characteristic length l_p ; the points are the calculated correlation function and the lines are fits to an exponential.29

Figure 3.3: Sample infiltration system showing all three species used in simulations.....31

Figure 3.2: (a) A cylindrical capillary with diameter $D = 9$, height $H = 100$, and polymer chains of length $N=10$ are used to simulate the process of polymer wicking. At $10^{-3} \tau_{LJ} = 1$, the polymers are held outside the capillary by unfavorable interactions but can still fluctuate as a free surface at the mouth of the capillary. For $t > 0$, the interactions between capillary and polymers are turned up to induce wicking into the capillary. (b) the height of the polymer interface can be tracked by fitting a sigmoidal function to $\rho(z)$. The full system showing the polymer film beneath the pore is shown in Supplemental Information.....32

Figure 3.4: Infiltration height as a function of time. The scaling at early times is consistent with the inertial regime, while the scaling at later times appears to approach the Lucas-Washburn (LW) scaling.33

Figure 3.5: (a) Contact angle simulations are used to parameterize the relationship between the interaction energy (ϵ_{pc}) and contact angle (θ). ϵ_{pc} varies approximately linearly with $\cos\theta$ for all values of N . (b) The dependence on chain length N is explained by the molecular weight dependence of the surface tension (γ) from Ref [55] and the work of adhesion from the Young-Dupré equation for $\epsilon_{pc} = 0.5$. The work of adhesion measured is $W_{ad} = 0.155 \epsilon/\sigma^2$. Literature[56] reports similar values for LJ polymers.....35

Figure 3.6: Height trajectories of flexible polymer chains of length $N = 50$ show that the polymers only infiltrate past their mean squared end-to-end distance (black line) if $\theta < 84^\circ$. The pore diameter D is 5σ37

Figure 3.7: (a) Critical contact angle versus chain length, N , and (b) degree of confinement, δ . The critical angle for infiltration of flexible chains plateaus around a value of 83° whereas the critical value for stiff chains plateaus around 77° . The dashed lines indicate theoretical predictions from the energy balance. (c) Diagram showing how change in height, dh , relates to pore geometry and free energy.38

Figure 3.8: (a) The biased potential of mean force is computed from the probability distribution of $z - z_0$ produced by the umbrella sampling simulations. (b) Subtracting the biasing potential from the PMF provides free energy curves with unknown additive constant.....40

Figure 3.9: (a) Specifying the offsets for free energy curves manually allows us to roughly reconstruct the full free energy curves. I observe that for the 6 different contact angles the slope of the free energy switches signs. (b) Fitting a line to the slopes of the free energy curves vs contact angle allows us compute the critical contact angle ($\approx 82^\circ$). Error bars are computed from replicates and multiple sampling windows.40

Figure 3.10: (a) Simple fluid infiltration h vs t (b) Simple fluid h vs θ for select time points showing that infiltration appears to stop at 90° . (c) $N = 5$ infiltration h vs θ for select time points. Infiltration appears to stop just above 80° . (d) Critical contact angle values for different chain lengths.45

Figure 4.1: Variation of meniscus curvature, resistance to liquid flow, tube radius, free energy as the liquid penetrates the tube and the accompanying power consumption by the liquid during penetration are plotted as a function of position in the sinusoidal tube. At the constrictions, marked by an arrow, the curvature of the meniscus, resistance to flow and power consumption increase. The free energy decreases monotonically as penetration proceeds. These calculations were for silicone oil ($\eta = 971$ cP, $\gamma = 21.2$ dyn cm⁻¹, $\theta = 20^\circ$)[37].49

Figure 4.2: (a) A wavy capillary is characterized by its amplitude, A , radius, R , and wavelength, λ . (b) The free energy in a wavy capillary has 3 main contributions: polymer confinement (orange), free surface expansion and contraction (red), and wetting (green). (c) By changing the relative importance of each term, barriers can be introduced into the free energy profiles. Increasing the contact angle, θ , reduces the role of wetting and halts infiltration.....51

Figure 4.3: $\lambda = 4$, $A_0 = 3$ has rapidly changing cross-section and barriers exceeding $k_B T$ by $\sim 10^2$. (b) $\lambda = 16$, $A_0 = 2$ has a slowly changing cross-section with no barriers in the total free energy. Changing the geometric parameters of the wall, I can artificially create energy barriers even under highly wetting conditions. Thus, some highly wavy walls would be resistant to infiltration of most imbibing fluids.....53

Figure 4.4: Free energy from theory predicts the presence of local minima and maxima that can vanish above a certain contact angle. The same is observed in

simulations for the contact angles of 0° , 84° , and 90° , however, the free energy barriers are lower than predicted.56

Figure 4.5: (a) At $\theta = 90^\circ$ infiltration is not observed at all. (b) At $\theta = 84^\circ$ infiltration is still observed, but proceeds stepwise jumping between minima, indicating that infiltration for this system is an activated process. (c) At $\theta = 72^\circ$ infiltration still proceeds stepwise, but individual jumps become harder to distinguish. (d) At $\theta = 40^\circ$ infiltration proceeds smoothly without jumping like would be expected in a Lucas-Wasburn system.....58

Figure 5.1: Schematic illustration of solvent-driven infiltration of polymer (SIP) into a NP film. A polymer/NP bilayer is annealed with solvent vapor, leading to capillary condensation of solvent in the NP packing, followed by swelling and infiltration of polymer[67].....64

Figure 5.2: Volume fraction of PS in the NP packing (ϕ_{PS}) (A) for PS ($M_n = 8000$ g/mol) into 23 nm particle packings (circles) and 77 nm particle packings (diamonds), after 30 min (closed) or 24 h (open) of vapor exposure for various solvents at different χ , and (B) using different good solvents ($\chi < \chi_c$) as a function of PS molecular weight after 30 min of vapor exposure[67]....65

Figure 5.3: Reduced tracer diffusion coefficients of dPS for (a) $M_n = 168$ (squares) and 532 (triangles) kg mol^{-1} or (b) $M_n = 1866$ (circles) and 3400 (inverse triangles) kg mol^{-1} in nanocomposites containing NR-long ($\phi_{NR} = 0-0.1$) exhibiting a monotonic decrease or a minimum of diffusion coefficients, respectively. Insets describe the local polymer diffusion in the direction parallel ($D_{||}$) and perpendicular (D_{\perp}) to NRs, depending on the relative size of

the R_{NR} to R_g ; (a) isotropic tracer diffusion ($D_{||} \cong D_{\perp}$) when $R_{NR} > R_g$ and (b) anisotropic tracer diffusion ($D_{||} > D_{\perp}$) when $R_{NR} < R_g$ [69].67

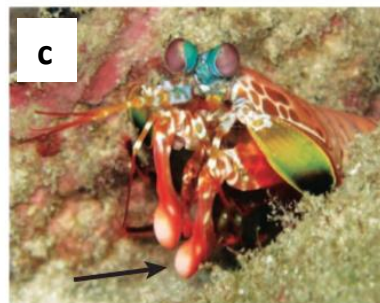
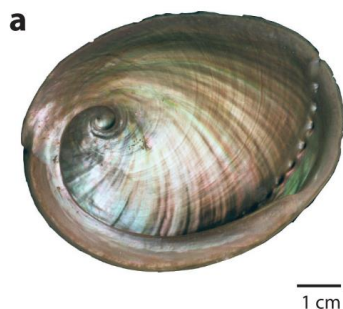
Figure 5.4: (a) Normalized viscosity ($\mu_{confined}/\mu_{bulk}$) obtained for PS undergoing CaRI at $T = 403$ K and the (b) ΔT_g ($T_g - T_{g,bulk}$) as a function of confinement ratio (CR). The lines are to guide the eye[21], [40].....68

Figure 5.5: Comparison between the experiment and the theory. The symbols are shown for the experimental data taken from reference [14]. The lines are from theoretical prediction of Equation (25). [48].....69

CHAPTER 1: Introduction

1.1 Nanocomposites with high filler fractions and their fabrication techniques

Nanocomposites are a class of materials that rely on microscopic mixing of polymers and nanofillers to impart increased strength, permeability, conductivity and other desirable features[1]–[3]. Although they were first understood using the rule of mixtures – which for example expresses the composite elastic modulus as a weighted average of the components by volume fraction – many studies show that nanocomposites exhibit properties that bely the strength of their components and the rule of mixtures[4], [5]. Many such nanocomposites can be found in nature, such as abalone nacre, bone, and the dactyl club of the mantis shrimp[6]–[9]. In each of these natural composites, their specific close-packed morphology and high proportion of inorganic nano-inclusions contribute to the uniquely enhanced properties of the composite. Nacre benefits from the interlocking of nanoplatelets and asperities on the surface to reduce pull out[10], [11], with polymers providing nano-bridging that prevents crack propagation[6].



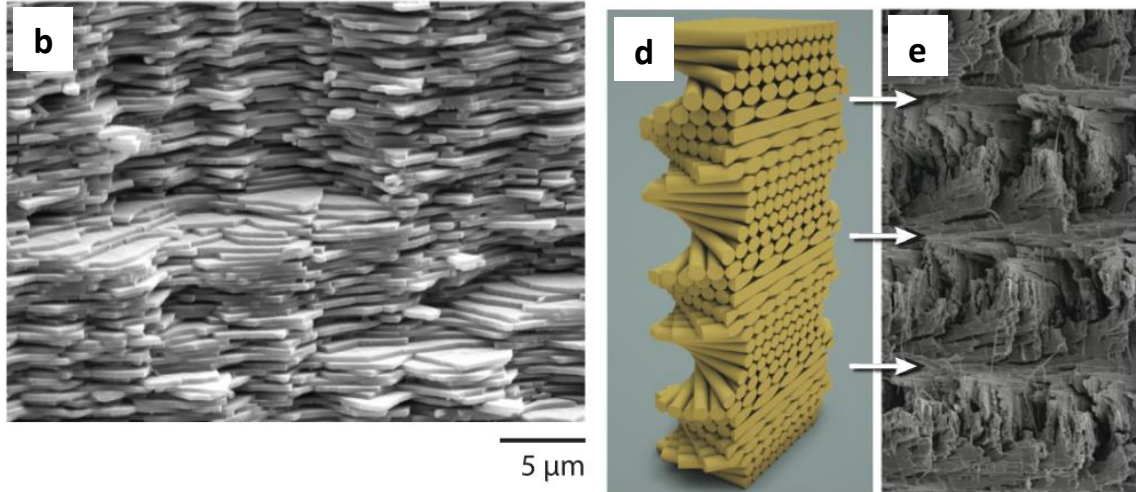


Figure 1.1: (a) – (b) Abalone nacre has a brick-and-mortar microstructure composed of brittle calcium carbonate glued together with small amounts of chitin. This structure has enhanced hardness and fracture toughness, two properties which are hard to achieve concurrently. (c) – (e) The dactyl club of the mantis shrimp has a helicoidal closed packed group of chitin fibers reinforced by mineralization as shown in the diagram and SEM micrograph. This structure provides excellent energy dissipation upon impact[9].

The addition of nanoparticles to polymer-based filtration membranes has also been shown to improve the trade-off between permeability and selectivity in gas separations[3], [12]. It is believed that this enhancement is caused by the disruption of chain packing in the polymer matrix which introduces free volume around the nanoparticles, improving the diffusion of the molecules through the membrane[3], [13]. It has been demonstrated using molecular dynamics that stiff polymers are more likely to pack loosely near particles, leading to an increase in the free volume. Prior studies on these membranes used small fractions of nanoparticles but indicated that ever increasing fractions of particles could provide even greater improvement to the membrane properties. Figure 1.2 shows the effect of adding fumed silica to a PMP film on the permeability of (a) the permeability of methane and (b) the permeability and selectivity of n-butane over methane; both plots show a marked increase in permeability.

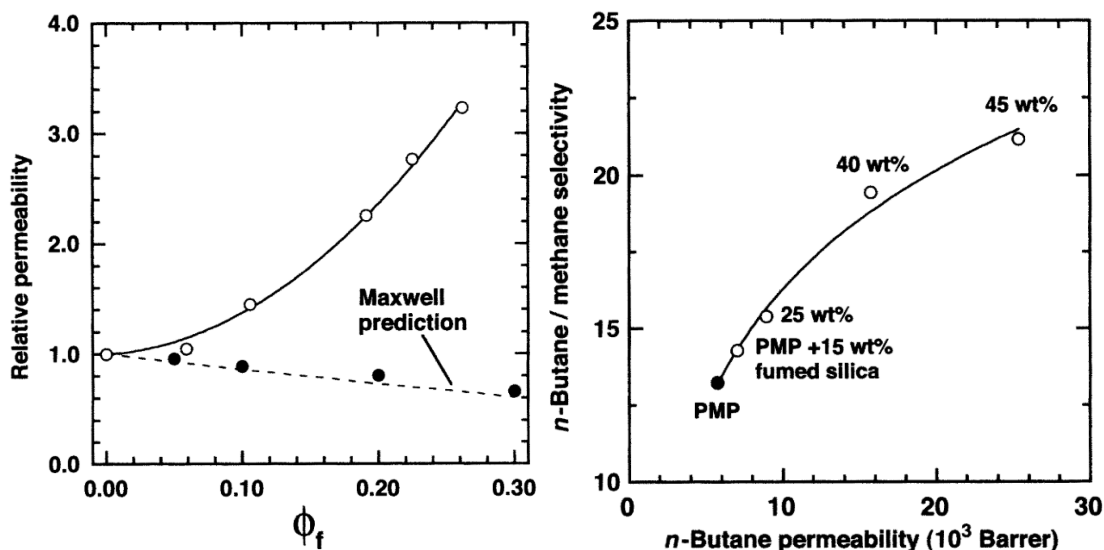


Figure 1.2: (a) The ratio of penetrant permeability in the nanocomposite to that in the pure polymer as a function of filler volume fraction. Filler volume fraction is estimated from $\phi_f = m_f / (m_f + m_p \rho_f / \rho_p)$, where m and ρ refer to the mass and density, respectively, of filler (f) and polymer (p) used in the nanocomposite. The dashed line represents the Maxwell model prediction[3]. Our data (open circles) are for methane permeation at 25°C in PMP containing nanoscale fumed silica (TS-530 from Cabot). Included for comparison are the data of Barrer et al. [14] for propane permeation at 40°C in natural rubber containing ZnO filler (solid circles). (b) The effect of fumed silica (TS-530) content on n-butane permeability and n-butane/methane selectivity of glassy PMP. These data were acquired at 25°C from mixtures composed of 98 mole % methane and 2 mole % n-butane at a feed pressure of 11.2 atm and a permeate pressure of 1 atm. [3]

Traditionally, nanocomposites are formed using several different techniques. One of the most widely used methods is polymer melt processing, which mixes nano-fillers into a polymer matrix using a blender. The downside to this method is that even small amounts of fillers cause the viscosity to sky-rocket, drastically increasing energy costs[4]. The fillers also have the unfortunate tendency to clump together rather than dispersing evenly[15], further complicating processing and compromising the nanocomposite's properties. Alternatively, layer-by-layer assembly (LbL) can be used to craft robust nanocomposites.

Although it is an industrially viable process, it can be time-consuming and tedious and is limited primarily to oppositely charged species and aqueous solvents[16], [17]. Another method to make nanocomposites is to infiltrate monomers or oligomers into a pre-assembled film and then polymerize the monomers to form a network[18]. Unfortunately, unlike in bulk polymerization, there is very little control over the reaction rate, polydispersity and local extent of the reaction under very high-confinement[4]. This leads to sub-optimal results such as low mechanical strength and loss of unpolymerized monomers/oligomers from the composite. Clearly, a better method is needed.

1.2 Capillary Rise Infiltration (CaRI)

A recently developed technique to produce nanocomposites with extremely high fractions of nano-inclusions uses capillary forces to infiltrate polymer into dense packings of nanomaterials. As previously shown, capillary rise infiltration (CaRI) is a highly effective technique for creating composites with extremely high filler fractions (>50 vol%) by inducing capillary infiltration of polymer into the interstices of nanoparticle packing above the glass transition temperature of the polymer [4], [19], [20]. This is typically implemented by first producing a bilayer of polymer and nanoparticles, which is subjected to heating to induce CaRI as shown in Figure 1.2. The method has proven to be remarkably robust as even polymers with extremely high molecular weight can be induced to undergo CaRI and several pairs of polymer and nanoparticles have been shown to be compatible with the process to produce nanocomposite films with an extremely high volume fraction of fillers (> 50%)[4], [21]. The method is especially attractive when nanocomposite films with anisotropic nanoparticles are desired.

Since CaRI uses capillary forces to induce mixing, mechanical energy is not required to create the nanocomposite. In fact, the energy necessary to induce CaRI is only used for heating. Additionally, by coating a polymer sheet with nanoparticles using die-slot coating in a roll-to-roll system, CaRI nanocomposites can be made highly scalable with very few steps compared to traditional LbL processing. CaRI nanocomposites also do not suffer from incomplete polymerization since the polymers are already fully formed before infiltration. Finally, CaRI is one of the few techniques that can produce polymer nanocomposites with filler fractions approaching those of natural nanocomposites.

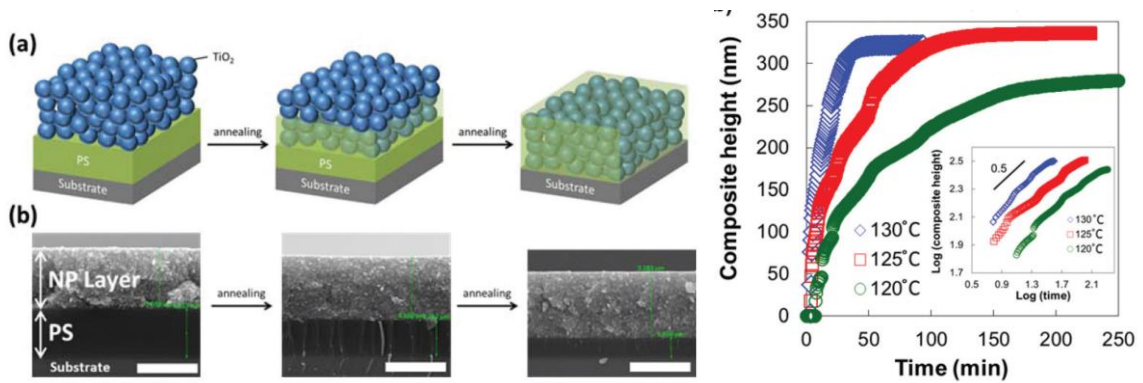


Figure 1.3: (a & b) Schematic and SEM micrographs of Capillary Rise Infiltration (CaRI) of polymers into nanoparticle packings. The process starts with a bi-layer thin film of nanoparticles and polymers that is then annealed above T_g of the polymers to induce wicking and form a composite layer (c) Infiltration dynamics of the polymers rising through the nanoparticle packing exhibit height vs time scaling consistent with the Lucas-Wasburn Equation[4].

1.3 Capillarity-induced Polymer Infiltration in Nanoscale Pores (< 100 nm)

In addition to the formation of nanocomposites, capillarity has been used to induce imbibition of polymers into small cylindrical pores in anodized aluminum oxide (AAO) membranes[22]–[24]. Different morphologies can be created by changing the wetting

conditions so that a pre-wetting film forms on the capillary surface [25]. The presence of a pre-wetting film makes it possible to produce hollow nanotubes, whereas the lack of a pre-wetting film results in a solid nanorod. These structures can then be freed from the membranes by dissolving the membrane in a mild acid or base solution.

Capillary driven infiltration of polymers in cylinders has also been studied using molecular simulations. These simulations not only displayed scaling consistent with the Lucas-Washburn equation, but also showed agreement between the independently calculated imbibition coefficient and the slopes of height versus time[26], [27]. They also note the presence of a slip length in the capillary that vanishes as fluid-wall interaction/wetting is increased.

The capillary rise of polymers in nanoscale pores has been shown to follow the scaling of the Lucas-Washburn equation – as shown in Figure 1.3[4]. The Lucas-Washburn equation describes the capillary driven infiltration of fluids into small pores and is derived by balancing the Laplace pressure with viscous dissipation[28]–[30]. Neglecting inertia and assuming fully developed laminar flow, Pouseuille’s law can be used to describe the rate of fluid imbibition

$$\pi r^2 \frac{dh}{dt} = \pi \Delta P \frac{r^4}{8\eta h} \quad 1.1$$

where r is the capillary radius, h is the height of the meniscus, ΔP is the pressure drop along the capillary length, and η is the viscosity. For pores of sufficiently small diameter, gravity can be neglected so that the pressure drop is determined only by the Laplace pressure across the interface

$$2hdh = \frac{2\gamma \cos \theta}{r} \left(\frac{R^2}{4\eta} \right) dt \quad 1.2$$

where γ is the surface tension and θ is the contact angle. Integrating from $h = 0$ @ $t = 0$ gives the Lucas-Washburn equation

$$h^2 = \frac{r\gamma_P \cos \theta}{2\eta} t \quad 1.3$$

A more general expression can be derived by including the effect of inertia, which can be important for infiltration at early times[31], [32]. This ensures that the initial fluid velocity and acceleration are not infinite near $t = 0$ as is the case for the Lucas-Washburn equation. The governing equation and boundary conditions for this problem, which was solved by Ichikawa and Satoda[32], balance inertia, capillary forces, and viscous forces

$$\left\{ \begin{array}{l} \rho[hh'' + h'h'] = \frac{2\gamma \cos \theta}{r} - \frac{8\eta}{r^2} hh' \\ h'(0) = 0 \\ h(0) = 0 \end{array} \right. \quad 1.4$$

where h is the penetration height, and ρ is the density. The solution to this initial value problem

$$h^2(t) = \frac{\rho r^3 \gamma \cos \theta}{16\eta^2} \left[e^{-\frac{8\eta}{\rho r^2} t} - 1 \right] + \frac{r\gamma \cos \theta}{2\eta} t \quad 1.5$$

contains two terms, one of which is the Lucas-Washburn equation at long times, and the second of which provides a decay time scale for the inertial regime. For early times, this exponential term reduces to $\frac{2\gamma \cos \theta}{\rho r} t^2$, which indicates height is linear in time until the

infiltration kinetics cross over into a roughly Lucas-Washburn-like regime with h^2 proportional to t .

When applied to packings, the Lucas-Washburn equation is often modified with a tortuosity factor to account for the meandering path of the pores. Some studies have also suggested that under confinement, it is necessary to use a slip length to describe the infiltration front[26], [33]. Taking into account these modifications, the Lucas-Washburn equation becomes $h^2 = \frac{(r+b)^2 \gamma \cos \theta}{4r\tau^2\eta} t$ where τ is the tortuosity factor and b is the slip length.

Finally, the Lucas-Washburn equation can be modified to account for pores with varying cross-section, such as sinusoidal capillaries[34]–[37]. Starting with the Navier-Stokes equations, assuming a parabolic velocity profile, and neglecting inertia gives

$$8\mu N_c(1 + V_c) \frac{dh}{dt} = 2\gamma \cos \theta - \rho g h r(h) \quad 1.6$$

where $\theta = \theta_e + \text{atan}\left(\frac{dr}{dz}\right)$ with θ_e as the equilibrium contact angle. The groups V_c and N_c represent the viscous term contributions from nonuniformity in the axial direction and the cross-sectional plane and are calculated using Eq 1.7 and 1.8

$$V_c = \int_0^h \left(\frac{dr}{dz}\right)^2 \frac{dz}{r^2(z)} \bigg/ \int_0^h \frac{dz}{r^2(z)} \quad 1.7$$

$$N_c = r^3(h) \int_0^h \frac{dz}{r^4(z)} \quad 1.8$$

Eq 1.6 – 1.8 do not explicitly rely on the functional form of $r(z)$ and can be used for any capillary with a non-constant cross-section. Since Eq 1.6 has no explicit analytical solution, it is typically integrated numerically.

1.4 Free Energy in confinement

The free energy of a confined flexible polymer is predicated on the random walk statistics of the polymer being preserved below the confining length scale. Thus, the chain forms blobs with dimension $D \approx bg^{1/2}$ where D is the capillary diameter, b is the kuhn length, and g is the average number of kuhn segments in a blob. Above the confining length scale, the polymer appears as a chain of blobs, with each blob contributing kT of energy to the chain. Thus, the confinement free energy $F \sim k_B T \left(\frac{N}{g}\right) \sim k_B T N \left(\frac{b}{D}\right)^2$ is proportional to the number of blobs, $\frac{N}{g}$, where N is the Kuhn length [38], [39]. This suggests that longer chains should experience confinement more acutely. Figure 1.4 shows the difference between applying this formulation of polymer confinement to real and ideal chains. In the ideal case, the polymer end-to-end distance along the capillary axis doesn't change, but for a real chain, it becomes extended. For a melt, the chain can be treated as ideal due to screening, but a solution would require that I consider a different scaling.

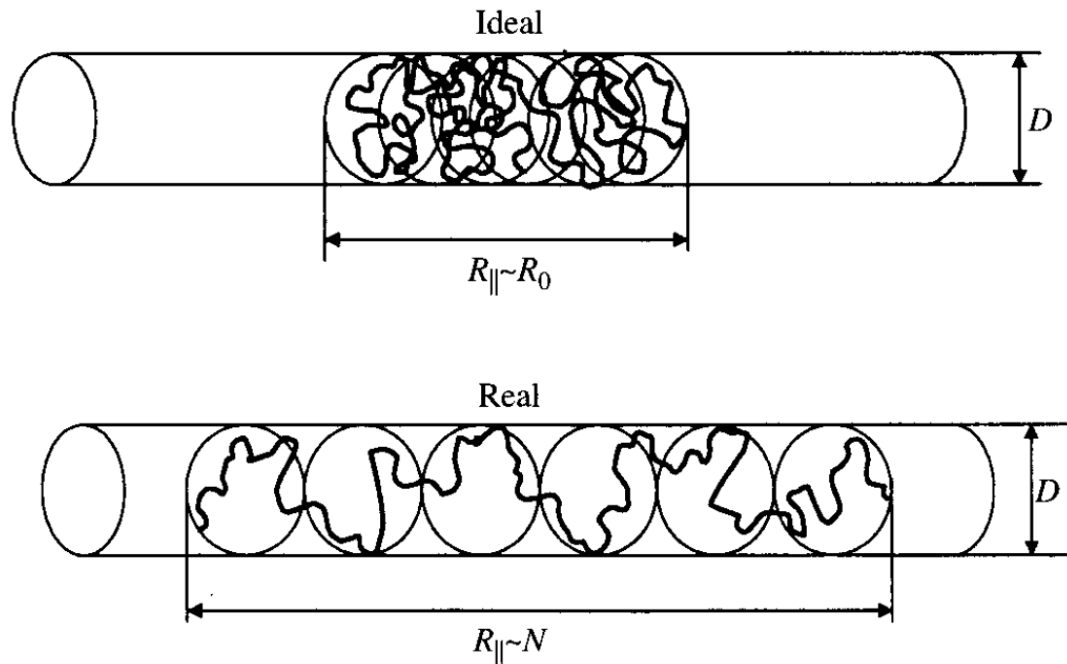


Figure 1.4: Real and Ideal chains under cylindrical confinement[38].

1.5 Unresolved topics in capillary rise of polymer in nanoscale pores

As summarized above, capillary rise of polymers into nanoscale pores is a versatile technique to produce nanocomposites with high filler fractions as well as nanoscale rods and tubes. Moreover, this approach provides a unique method to investigate the effect of extreme nanoconfinement on the dynamics and thermodynamics of polymers[40]. There are several unresolved fundamental aspects that require further investigation, some of which this thesis will address.

For example, it is not understood what happens to polymers in a CaRI nanocomposite when there is not enough polymer to fill the voids between particles. Recent experimental studies indicate that even very small quantities of polymer lead to significant reinforcement of spherical packings[20]. They also show that polymers tend to evenly disperse throughout

the entire nanoparticle packings to form three-phase composites, rather than stopping their infiltration once the polymer layer is depleted. Given the difficulties associated with directly observing the infiltration dynamics and resulting morphology in the CaRI composites, molecular dynamics simulations provides a powerful method to study CaRI under varying physicochemical conditions.

Another unresolved problem that has not been addressed is the effect of confinement on the ability of polymers to infiltrate the nanoparticle packing. The Lucas-Washburn equation predicts that infiltration is ultimately halted when the contact angle is 90. This is because there is no driving force for infiltration from the Laplace pressure across the interface. However, polymers under extreme confinement also lose conformational entropy due to the perturbation of the equilibrium conformation. In an infiltration system with extreme confinement and contact angles approaching 90°, the infiltration response is unknown. Given that confinement results in entropic loss of individual chains which also depends on the molecular weight of the polymer, the effect of significant confinement on CaRI is not fully understood.

Most treatments of both free energy and infiltration focus on pores with constant cross-section or treat large sets of random pores as if they can be described with an average pore size. Few papers investigate the effects of a varying cross-section on infiltration dynamics, although a few have derived new forms for the Lucas-Washburn equation in capillaries with sinusoidally varying radii[34]–[37], [41]. None so far, have attempted to describe how free energy of an infiltrating polymer changes in pores with varying cross-section. This could be useful in determining where bottlenecks in infiltration occur and may lead to new pathways for engineering packings that allow for better polymer infiltration.

1.6 Outline of this thesis

Understanding the capillary infiltration of polymer melts under extreme confinement is an invaluable asset to exploring the limits of the CaRI process. Fundamentally, it can also shed light onto more general problems of equilibrium and the connection between free energy and dynamics. In Chapter 2, I discuss the mechanism behind polymer reinforcement of nanoparticle packings using simulations of small fractions of polymers infiltrating and spreading into a packing of ellipsoids. In Chapter 3, I show how the critical contact angle above which infiltration is not possible depends primarily on the stiffness of a polymer chain rather than its length. In this chapter, I will also flesh out some free energy arguments which lead to a theoretical prediction for this critical contact angle. In Chapter 4, I extend my work with cylinders to wavy capillaries, and show that as a direct result of the sinusoidally varying cross-section that free energy barriers along their axis can be present. When those barriers are big enough, I observe different modes of infiltration. Finally, in Chapter 5, I discuss the outlook of my current work, and what still needs to be investigated afterwards.

CHAPTER 2: Molecular Dynamics Simulations of Undersaturated Capillary Rise Infiltration in Nanoparticle Packings

Reprinted in part with permission from J.L. Hor, Y. Jiang, D.J. Ring, R.A. Riggleman, K.T. Turner, and D. Lee, *ACS Nano* 2017, 11, 3229-3236. Copyright 2017 American Chemical Society.

2.1 Introduction

The CaRI process is useful for generating dense nanocomposites with exceptional strength and toughness. It can also be used to create porous 3-phase nanocomposites. This can be done simply by changing the relative thicknesses of the polymer and nanoparticle films in the initial bilayer such that there is not enough polymer to entirely fill the interstices between the nanoparticles. This process is called Undersaturated CaRI or UCaRI. Annealing for short times results in a gradient of polymer density along the height of the composite, and annealing for long enough can result in three phase composites with a uniform density of polymer throughout.

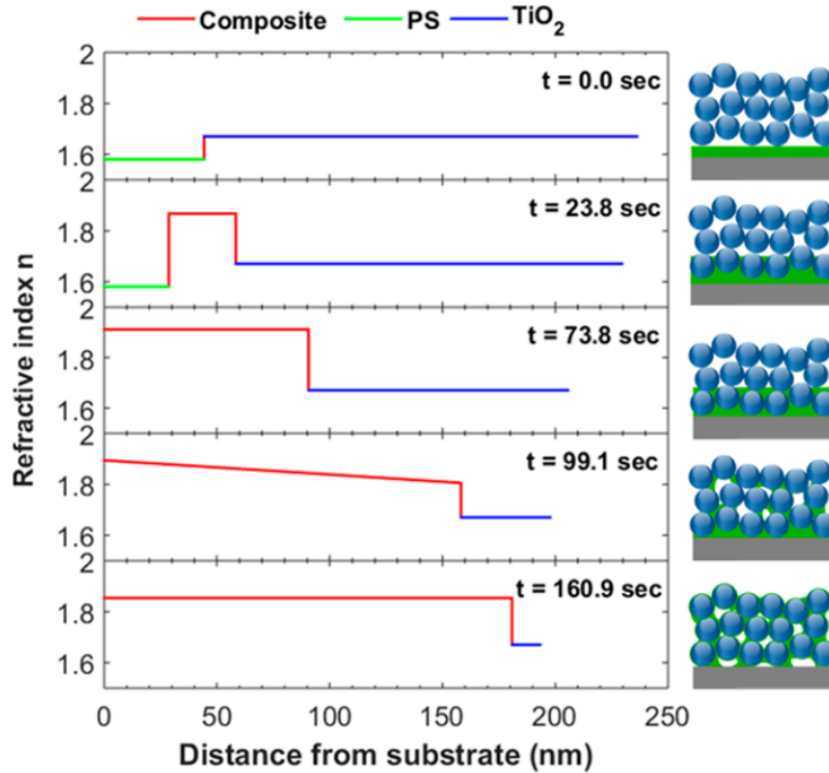


Figure 2.1: Refractive index of the film as a function of distance from the substrate at various annealing intervals, with the schematic illustration representing the film morphology at each stage. The bilayer film composed of a 190 nm TiO_2 NP layer ($n_{\text{NP}} = 1.67$) on a 45 nm PS layer ($n_{\text{PS}} = 1.58$) is annealed at 150°C [20].

Experimental work with bi-layer films of Titania nanoparticles and polystyrene has been conducted and indicates that either a graded or uniform porous composite film can be produced by varying the time of thermal annealing. The height and refractive index of the bi-layers were monitored *in situ* for different polymer fractions using ellipsometry as shown in Figure 2.1. The height of the polymer film decreases over time while a composite layer forms; the sum of the heights of the composite and nanoparticle films is constant over time. After the polymer film is completely depleted, the pure nanoparticle fraction continues to decrease while the thickness of the composite layer increases over time,

indicating the polymer continues to spread further into the nanoparticle packing. This is further confirmed by a change in contact angle of a water droplet placed on top of the film before and after annealing. An analysis of the refractive index indicates that a gradient develops after the polymer layer is initially depleted and that it gradually disappears after further annealing. These composites could be extremely useful for creating membranes for separation processes, ion conduction, or as strong lightweight materials.

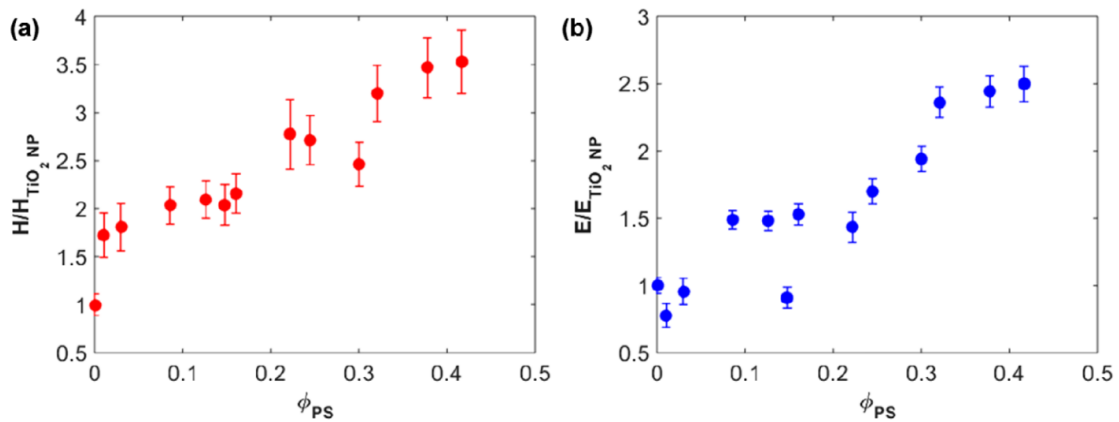


Figure 2.2: Mechanical properties of the nanoporous PINFs measured using nanoindentation tests. (a) The normalized hardness and (b) the normalized modulus of the composite increase with the PS volume fraction (ϕ_{PS}). Every data point is expressed as a statistical average of nine partial loading cycles with loads 40–500 μN at 49 random spots on the sample, with indent depths of 100–200 nm. The error bar represents the standard deviation of the mean. The TiO_2 NP film’s hardness and reduced modulus are 271.6 ± 21.4 MPa and 12.9 ± 0.5 GPa, respectively, whereas the PS film’s hardness and modulus are 292.2 ± 28.9 MPa and 6.9 ± 0.3 GPa, respectively[20].

Mechanical testing of these porous and gradient films in Figure 2.2 indicates that the neat nano-particle films are reinforced by even very small fractions of polymer (< 5 vol%). This seems to indicate that the polymers act to glue the nanoparticles together. However, it is not understood how the polymer acts to hold the nanoparticles together, especially at

such low volume fractions. Additionally, while the infiltration process seems to follow Lucas-Washburn like dynamics at first, after the polymer layer is depleted it continues to spread by a different mechanism. In order to find the answer to these two problems, I use molecular dynamics (MD) to simulate the undersaturated infiltration process and to investigate how polymers glue together nanoparticles in the final composite.

2.2 Model Parameters and Methods

The MD simulations are performed using the molecular dynamics simulation package LAMMPS with a similar approach as previously described.[19] All quantities are calculated in reduced units specified by the Lennard-Jones (LJ) parameters ϵ and σ which denote the interaction strength and size, respectively, of a LJ unit. The interactions between all non-bonded units are described by the 12-6 LJ potential with cut-off radius 1.75σ

$$U_{LJ}(r_{ij}) = 4\epsilon_{ij} \left[\left(\frac{\sigma_{ij}}{r_{ij}} \right)^{12} - \left(\frac{\sigma_{ij}}{r_{ij}} \right)^6 \right] - 4\epsilon_{ij} \left[\left(\frac{\sigma_{ij}}{r_{cut}} \right)^{12} - \left(\frac{\sigma_{ij}}{r_{cut}} \right)^6 \right]$$

All ϵ_{ij} and σ_{ij} values are unity to reflect neutral interactions between the NP, substrate, and the polymer monomers. The substrate is a flat surface of randomly packed LJ sites. Each polymer chain consists of 10 bonded Lennard-Jones (LJ) sites, where adjacent monomers interact through a harmonic bond potential $U_b(r) = \frac{k}{2}(r - \sigma)^2$ with spring constant $k = 2000 \frac{\epsilon}{\sigma^2}$. Each ellipsoidal nanoparticle is treated as one rigid molecule composed of 4684 LJ sites arranged in a shell with dimensions 25σ by 50σ .

Polymer films are created following a procedure described by Kremer and Grest[42], [43]. First, polymers are generated in a box with the same dimensions as the final film by

assuming a density of approximately 0.85. They are generated by using a random walk, where each step corresponds to one bond of length $l = 0.97\sigma$ and the bond angle is chosen at random between the angles $27^\circ - 333^\circ$. This condition ensures that bonds cannot fold back on each other and that the polymers are close to their equilibrium dimension. Additionally, the polymers are also constrained to reflect off the boundaries in the z -direction. This keeps them inside the box in that direction so that reflective boundary conditions can be applied to the top and bottom to form a film. The other 2 dimensions use periodic boundaries to simulate a pseudo-infinite film. These random films contain many overlaps which must be removed before equilibrating, otherwise the simulation will crash. Overlaps are removed by using a sinusoidal pair potential $u(r_{ij}) = A \left[1 + \cos\left(\frac{\pi r}{r_c}\right) \right]$ and ramping the value of A gradually. After running for 100 time steps, it is safe to switch to the LJ pair potential. The films are then equilibrated for multiple diffusion times using a bond-swapping algorithm to increase the speed of equilibration.

The nanoparticle packing is formed by annealing an array of 54 nanoparticles at $T = 25 \frac{\epsilon}{k_B}$ and then compressing it to an xy cross-section of 100σ by 100σ to produce a dense packing of nanoparticles with packing fraction ≈ 0.6 . Periodic boundaries are used in the xy -plane to simulate an infinitely extended packing. The packing is then placed on top of a film of the equilibrated polymers with half the number of LJ units necessary to fill the packing voids. The whole system is then annealed at $T = 0.7 \frac{\epsilon}{k_B}$ to induce infiltration into the packing.

2.3 Infiltrating Films and Analyzing Polymer Distribution

Images from before and after the infiltration process as shown in Figure 2.3a indicate visually that polymer has infiltrated all the way to the top of the nanoparticle packing. The monomer density profile $\phi_{poly}(z)$ at different times during the infiltration is shown in Figure 2.3b, demonstrating the depletion of the polymer film and near homogenization of the NP film; residual variations in the density along the z-axis are due to variations in the porosity of the packing due to the finite size of the simulation box.

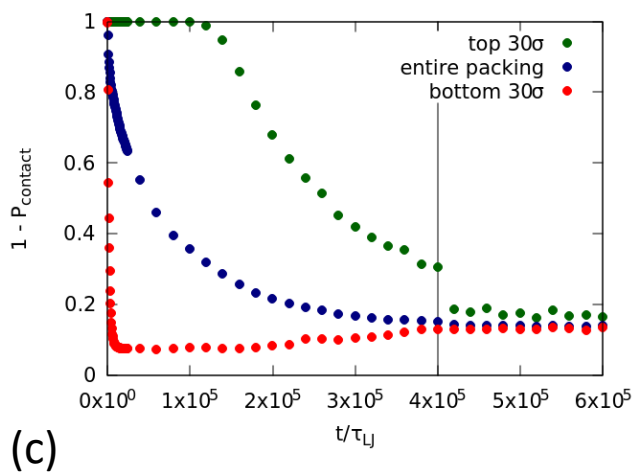
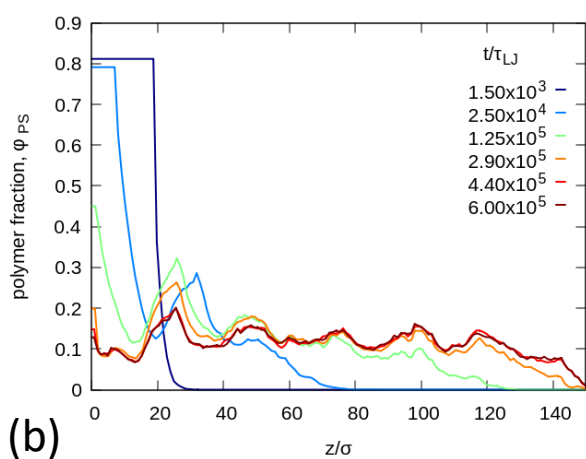
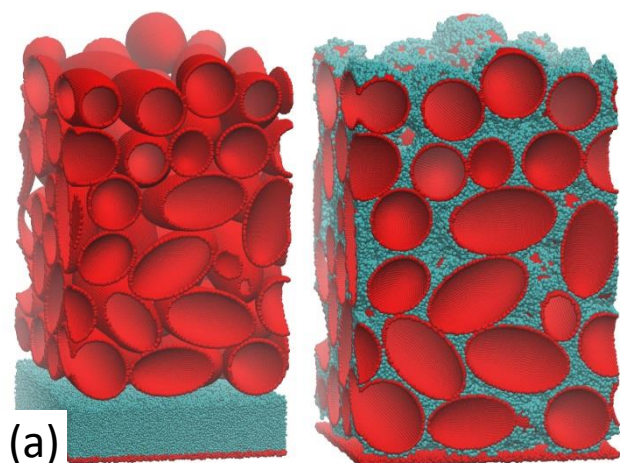


Figure 2.3: (a) Polymer/NP bilayer film prior to annealing (left) and the PINF after annealing (right). (b) The local polymer density profile along the z-axis with annealing time shows that the polymer infiltrates and gradually distributes throughout the NP packing to form a uniform PINF. (c) Probability that a bead on the surface of the NPs is not in contact with a polymer monomer as a function of time. The bottom 30 σ is closest

to the polymer film, and the rapid decrease in the probability indicates that this layer of NPs quickly becomes covered with polymer, and the UCARI film gradually homogenizes with equilibration. Homogenization is accelerated by increasing the temperature from 0.7 to 1.0 around $4 \times 10^5 t/\tau_{LJ}$.

To demonstrate that UCARI occurs in two stages, I calculate the probability that one of the NP surface sites is bare (i.e., not in contact with a polymer monomer) as a function of time, $1 - P_{\text{contact}}$. From the results in Figure 2.3c, I observe that when I average over the entire packing, $1 - P_{\text{contact}}$ monotonically approaches its equilibrium value. However, the top and the bottom of the packing exhibit distinct behaviors from each other. The top of the packing also monotonically approaches its equilibrium value, while the NPs near the bottom are quickly covered with polymer ($1 - P_{\text{contact}}$ tends to 0). As the polymer homogenizes through the film, $1 - P_{\text{contact}}$ calculated in the bottom portion of the film then increases and approaches the value averaged over the whole film.

In order to further characterize the morphology of the UCARI films, I calculate the probability of observing a single polymer chain in contact with more than one nanoparticle at a time, P_{bridging} , for different fill fractions as shown in Figure 2.4. The value of P_{bridging} for each fill fraction is nearly constant with time since the simulations start from a fully infiltrated system with different fill fractions generated by removing polymer chains at random. Thus, they equilibrate rapidly to form the configurations shown on the right. It is clear from the plot that larger fill fractions have lower values of P_{bridging} , indicating that polymers move to points of contact between nanoparticles first before filling in the larger voids around the nanoparticles. This is visually evident in the images as well, especially for the lowest fill fraction which has a green border. Polymers prefer to bridge particles

because the regions near particle-particle contacts allow them the most polymer-particle contacts, effectively, increasing the fraction of their surface area in contact with another species.

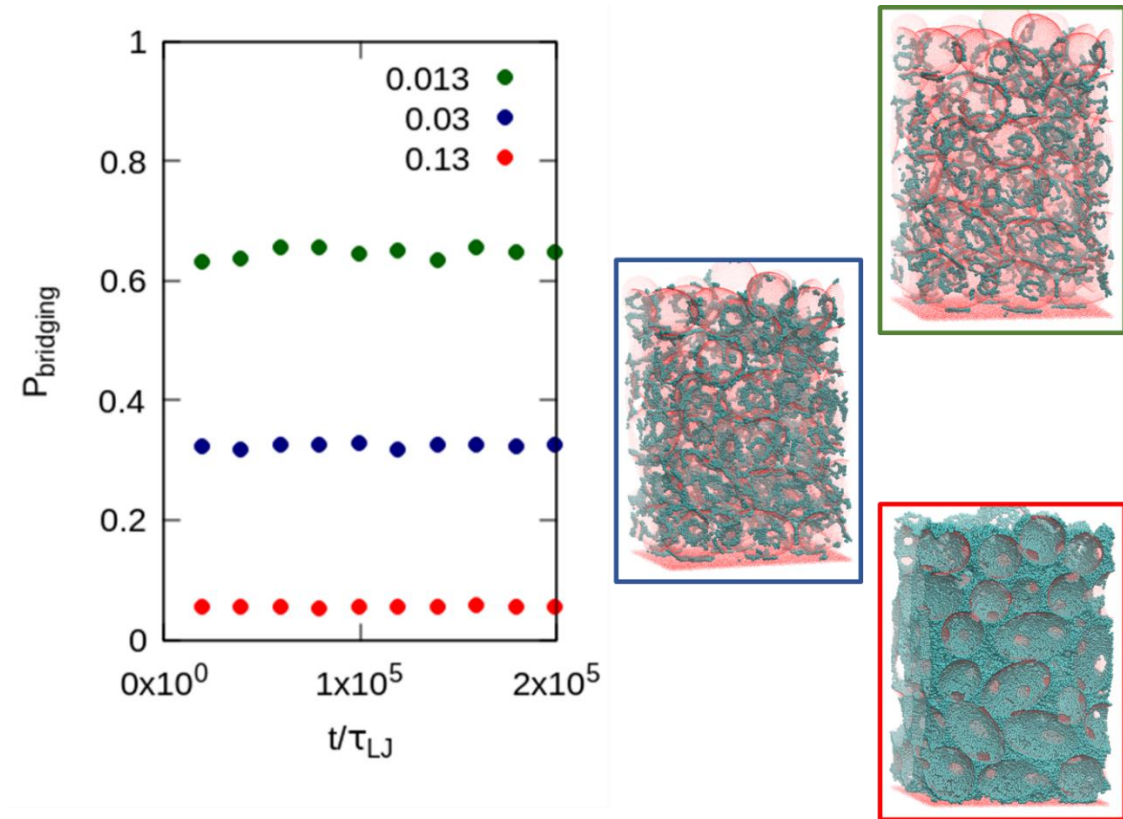


Figure 2.4: The probability that a polymer chain is in contact with two nanoparticles (P_{bridging}) for three different polymer fractions ($\phi_{\text{poly}} = 0.013, 0.03$ and 0.13). P_{bridging} increases drastically with lower ϕ_{poly} , suggesting the accumulation of polymer chains near particle contacts. Visualizations of each trajectory show that in lower fraction PINFs, the polymers form rings around nanoparticle-nanoparticle contacts.

2.4 Infiltration dynamics and surface spreading

To quantify the height of the nanocomposite (height of polymer-infiltrated front), I integrate the local polymer density $\rho(z)$ along the z axis up to a threshold value $f_{\text{cut-off}}$ of total integrated density ρ_T , and calculate the infiltrated height h such that:

$$f_{cut-off} \rho_T = \int_0^h \rho(z) dz$$

I track the infiltrating front using threshold values of 85% and 99%, which reflect the bulk and surface front of infiltrated polymer layer thickness in the NP packing, respectively. The slopes of h^2 vs t in Figure 2.5 suggest that infiltration is initially consistent with Lucas-Washburn like dynamics before the polymer can feel the top surface of the packing. From the 99% cut-off trajectory, I observe two linear regions where the transition from region I to region II corresponds to the depletion of the polymer layer. Two regions are also observed in the 85% cut-off trajectory. The change in slope from region II to region III, as determined from pictures of the trajectory, coincides with the dewetting of the bottom substrate. After these regions, the slopes continue to decrease due to the gradual homogenization of the nanocomposite.

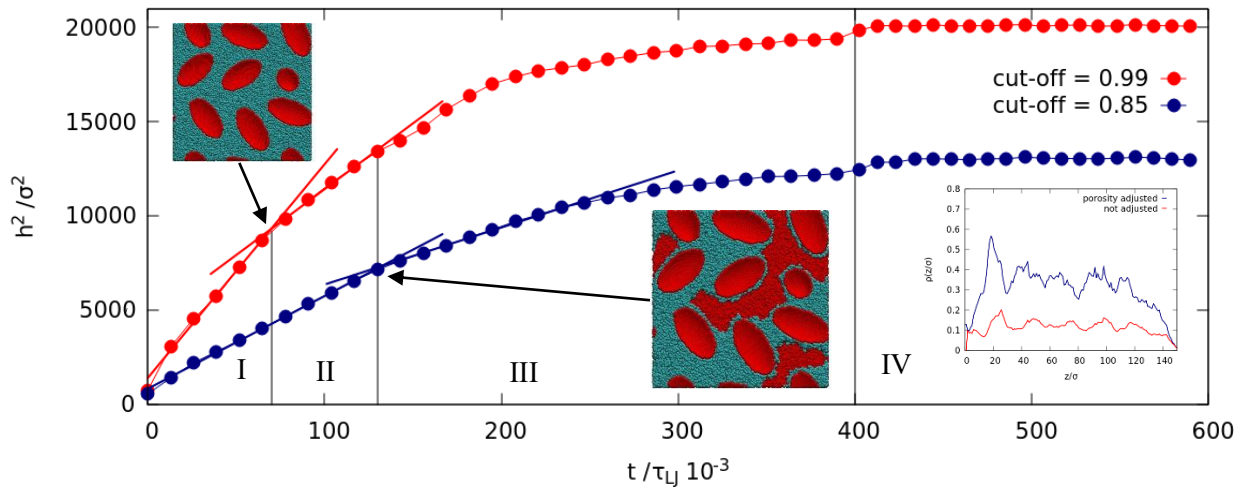


Figure 2.5: The height squared of the composite layer for the 85% and 99% cut-offs showing various linear regions with changing slopes, indicative of a transition in infiltration mechanism as (1) polymer infiltrates via capillary rise consistent with the Lucas-Washburn model, (2) polymer layer is depleted and polymer spreads via a slower surface diffusion behavior, (3) polymer has distributed throughout the packing and the

trajectory stops evolving. (4) end of trajectory showing that infiltration has stopped (annealed at $T = 1$). The inset shows $\rho(z)$ at the end of the trajectory to demonstrate that the polymer has spread throughout the entire nanoparticle packing uniformly.

Due to the slow evolution of the height profiles and incomplete homogenization, the temperature is ramped to $T = 1.0 \frac{\epsilon}{k_B}$ in region IV and annealed until the height stops evolving. From the inset of the local density, the polymer appears to be homogeneously distributed throughout the packing.

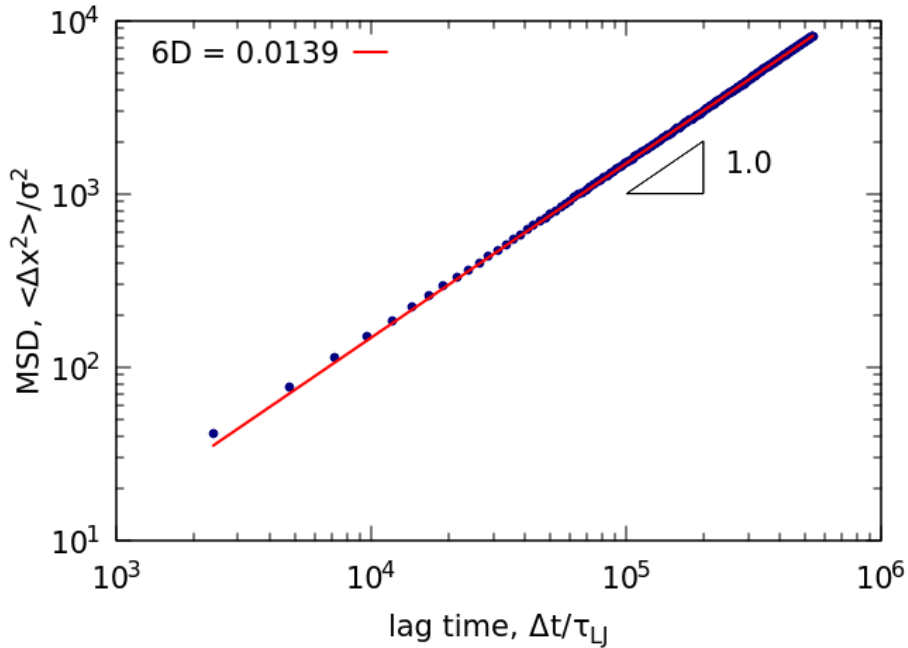


Figure 2.6: Mean squared displacement of polymers with 10 chain repeat units.

To determine the infiltration mechanisms present during UCaRI, the imbibition coefficient $C = \frac{h^2}{t} = \frac{R\gamma \cos \theta}{4\tau^2 \eta}$ from the Lucas-Washburn equation is independently estimated using the values shown in Table 2.1 and then compared to the slope observed in the simulations. The diffusion of polymers in the bulk is also calculated from the MSD as

a measure of the random motion of the polymers due to thermal fluctuations. Although this is not a directly applicable measure of thermal motion since the polymers are infiltrating along the surfaces of nanoparticles, it is not clear that planar diffusion would be directly applicable either due to the complex 3d structure of the composite. Additionally, the polymers have the same interaction strength with the nanoparticles as with each other and studies of planar diffusivities in supported thin films have shown that there can be good agreement between bulk and 2d planar diffusivities[19].

From this calculation, the imbibition coefficient varies between $0.007 - 0.245 \frac{\sigma^2}{\tau_{LJ}}$ and the slopes calculated at $t/\tau_{LJ} = 0$ and $t/\tau_{LJ} = 4 \times 10^5$ from Figure 2.5 are 0.113 and 0.008, respectively. The diffusion coefficient, D of this polymer is calculated from the MSD shown in Figure 2.6 to be $0.0025 \frac{\sigma^2}{\tau_{LJ}}$, which is comparable to the slope at $t/\tau_{LJ} = 4 \times 10^5$. It is tempting to assume that since the slope at $t/\tau_{LJ} = 4 \times 10^5$ falls within the range of imbibition coefficients calculated that it must be due to capillarity. However, the range of imbibition coefficients does not indicate which values are likely to be most representative of the actual imbibition. For example, the tortuosity range varies between 1 and 3 since we have no good way to extract the exact tortuosity from the packing. It is most likely that the tortuosity is closer to 3 than 1, however, since the polymers can follow many different non-straight paths through the packing. Additionally, if we attempt to better estimate the viscosity by interpolating between the viscosity values used, we would expect a viscosity on the lower range, since $N=10$ is closer to 5 than 50. Therefore, the lower bound could be too low by almost an order of magnitude.

Table 2.1: Quantities used in the calculation of the imbibition coefficient

R/σ	5
$\frac{\gamma}{\epsilon/\sigma^2}$	0.39 – 0.49 [†]
$\cos \theta$	1
$2\tau^2$	1 – 3 [†]
$\frac{\eta}{\epsilon\sigma^2/\tau_{LJ}}$	5 – 50 [†]

[†]values from Shavit *et al.*

2.5 Summary

Undersaturated infiltration follows the Lucas-Wasburn equation until the entire polymer film is depleted, at which point it begins to spread throughout the packing along the surfaces of the nanoparticles via surface diffusion. Furthermore, I determined that the polymers tend to create bridges between particles near their point of contact. I hypothesize that this is to minimize their exposed surface area and increase their total contacts with nanoparticles and other polymers. This phenomenon is analogous to the formation of capillary bridges in sandcastles. These bridges have been shown to dramatically enhance the mechanical properties of nanoparticle packings even at low fill fractions.

CHAPTER 3: Critical Contact Angle to Induce Capillary Rise of Polymers in Nanopores Does Not Depend on Chain Length

Reprinted with permission from D.J. Ring, R.A. Riggleman, and D. Lee, *ACS Macro Lett.* 2019, 8, 31-35.

Copyright 2019 American Chemical Society.

3.1 Introduction

Capillarity-driven flow of polymers in cylindrical tubes with nanoscale pores enables fabrication of novel nanostructures such as nanotubes and nanorods and at the same time provides a versatile method of confining polymer chains under physical confinement.[25], [44] Prior work has reported changes in the translational and segmental dynamics of polymers in cylindrical nanopores[45] as well as changes in glass transition temperature of semicrystalline polymers.[23] Cylindrical confinement also has a significant impact on the phase behavior of block copolymers[46] and semicrystalline polymers.[29] Many of these observed changes in the morphology and dynamic behavior of polymers under nanoscale confinement is attributed to the changes in polymer configurations.[38], [47] That is, when the characteristic dimension of unperturbed polymer chains such as their end-to-end distance (R_e) is comparable to or greater than the diameter of the pores, chains lose significant entropy, affecting their behavior.[48]

Experimental results as well as molecular dynamics (MD) simulation of capillary imbibition of polymers into nanoscale pores have shown that infiltration dynamics can be described using the Lucas-Washburn theory, $h = \sqrt{\frac{D\gamma \cos \theta}{4\eta} t}$, which describes the capillary infiltration dynamics of liquids with viscosity η and surface tension γ wicking into pores

of diameter D . [26], [28], [30] The critical parameter that determines whether a liquid would undergo capillarity-driven imbibition into a pore is the contact angle θ of the liquid on the pore surface. The model indicates that as long as θ is less than 90° , the liquid will undergo capillarity-driven flow into a pore. For polymers where the pore diameter is smaller than R_e , there is an intriguing possibility that the critical angle for infiltration to occur could be less than 90° since the polymer chains would require additional thermodynamic driving force (i.e., more favorable wetting) to overcome loss of conformational entropy. Studies of infiltration have used polymers and series of alkanes of different lengths to probe the influence of pore geometry, wetting, and boundary effects on infiltration behavior, but have not closely examined the effects of chain entropy on infiltration. [26], [30]

In this study, I use molecular dynamics (MD) simulations to investigate how physical confinement of polymers in nanoscale cylindrical pores impacts the capillarity-driven infiltration of polymers into the nanopores. In particular, I study the impact of chain confinement on the critical contact angle (θ_c) above which infiltration of polymers into nanopores ceases to occur. To enable this study, I find the relationship between the contact angle of polymer on the solid surface and polymer-surface interactions for a range of polymer chain lengths. By varying the pore diameters, polymer chain length and statistical segment sizes, I systematically probe the effect of confinement on infiltration of polymers into cylindrical nanopores. Somewhat unexpectedly, the critical contact angle does not strongly depend on the confinement ratio $(R_e/D)^2$ as the size of the chains becomes comparable to or larger than the pore size. A simple free energy argument shows that the critical angle for infiltration depends strongly on the size of statistical segments rather than the total chain length, consistent with my simulation results.

3.2 Model details and system setup

I use a bead-spring model with Lennard-Jones particles, harmonic bonds, and harmonic bending potentials to model my coarse-grained polymers.[19], [49], [50] By adding the angle potential $u(\theta) = \frac{k_\theta}{2}(\theta - \theta_0)^2$ I can model both fully flexible chains ($k_\theta = 0$) and semi-flexible chains ($k_\theta = 10$) having a bond angle of $\theta_0 = 2\pi/3$. This allows us to simulate polymers with different statistical segment sizes to investigate the effect of backbone rigidity on the critical contact angle of capillary rise.

In order to compute the persistence length for polymers with different statistical segment sizes, I computed the bond autocorrelation function for each polymer. The bond autocorrelation $\langle r_i \cdot r_j \rangle = \exp\left(-\frac{|i-j|\sigma}{l_p}\right)$ is calculated in Figure 3.1 by averaging over all chains and the projections of some bond vector, r_i , onto all other bond vectors, r_j , along the chain backbone. Since the autocorrelation decays exponentially along the backbone, I can extract the characteristic decay length as the persistence length, l_p .

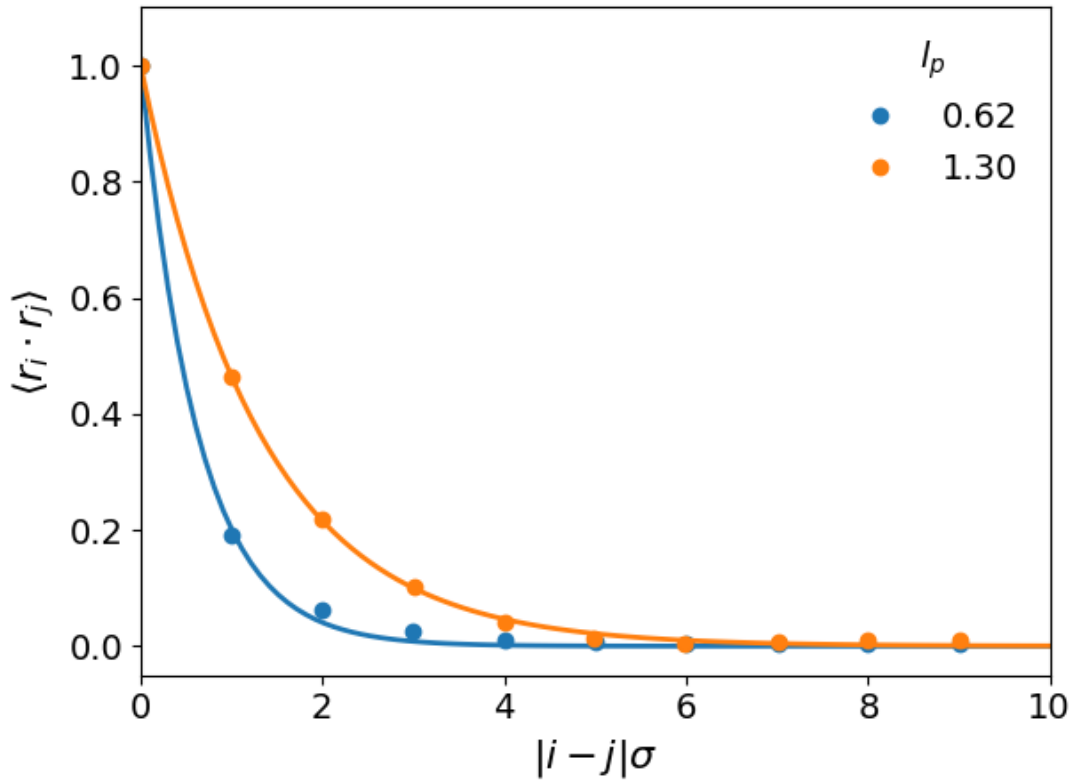


Figure 3.1: The bond autocorrelation function decays exponentially with characteristic length l_p ; the points are the calculated correlation function and the lines are fits to an exponential.

Table 3.1: Measures of chain stiffness for fully flexible and semi-flexible chains

k_θ	$2l_p/\sigma$
0	1.24
10	2.62

All polymer melts are formed from collections of overlapping chains with approximately Gaussian statistics.[49] Overlaps are removed by ramping a soft cosine interaction potential in place of the standard LJ potential before equilibrating the polymer melts with their actual interaction potentials.[42] All melts are equilibrated such that they

diffuse on average by their chain dimension, R_e , which can be calculated from a comparatively short simulation. All surfaces are composed of LJ sites arranged in a 2d triangular lattice with lattice spacing $l = 0.91$. Non-bonded interactions are controlled with the cut and shifted LJ potential $u_{ij}(r) = 4\epsilon_{ij} \left[\left(\frac{\sigma_{ij}}{r} \right)^{12} - \left(\frac{\sigma_{ij}}{r} \right)^6 \right] - 4\epsilon_{ij} \left[\left(\frac{\sigma_{ij}}{r_c} \right)^{12} - \left(\frac{\sigma_{ij}}{r_c} \right)^6 \right]$ where $r_c = 1.75$ is the cut-off distance and ϵ_{ij} represents the interaction strength between atoms i and j . All simulations are performed at $T/T_{LJ} = 0.7$ unless otherwise specified.

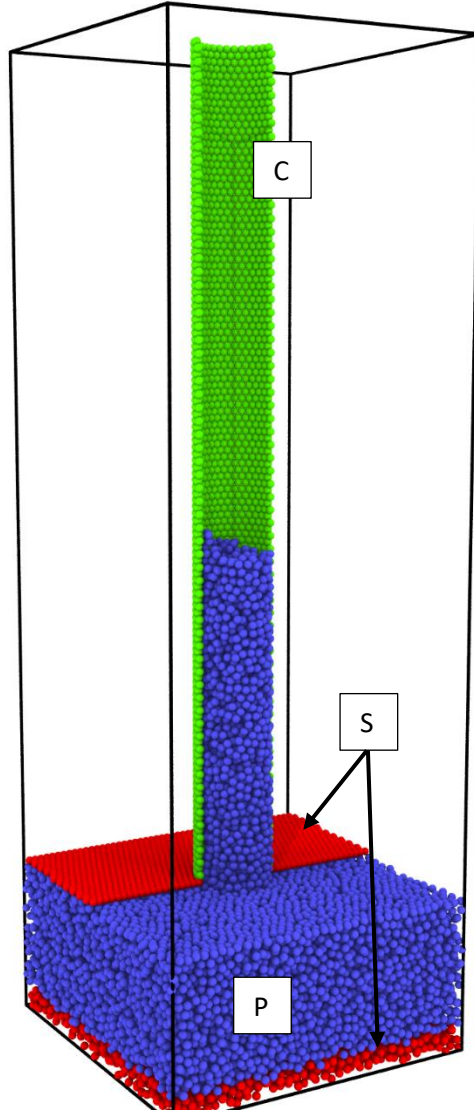


Figure 3.2: Sample infiltration system showing all three species used in simulations.

A sample infiltration system in Figure 3.2 shows the 3 main species, polymer (Blue), capillary (Green), and substrate (Red). Their non-bonded interactions are shown in the table with samples values corresponding to an infiltrating system. While σ is kept the same for all 3 species, ϵ is adjusted for the interactions between polymer and capillary (P-C) in order to adjust the polymer contact angle and start or halt infiltration. The capillary (green) and top surface (red) are allowed to move vertically to maintain contact with the surface of the melt.

Table 3.2: LJ Parameters for infiltration

Species	ϵ	σ
Red-blue (S-P)	1.00	1.00
Blue-green (P-C)	0.611	1.00
Blue-Blue (P-P)	1.00	1.00

Prior to performing the infiltration simulations, I reduce ϵ_{PC} between the LJ particles that comprise the polymer (P) monomers and the capillary (C) sites to a non-wetting value so that the polymer-vapor interface can relax near the opening of the capillary. Subsequently, I increase ϵ_{PC} and test whether I observe spontaneous infiltration as shown in Figure 3.3a.

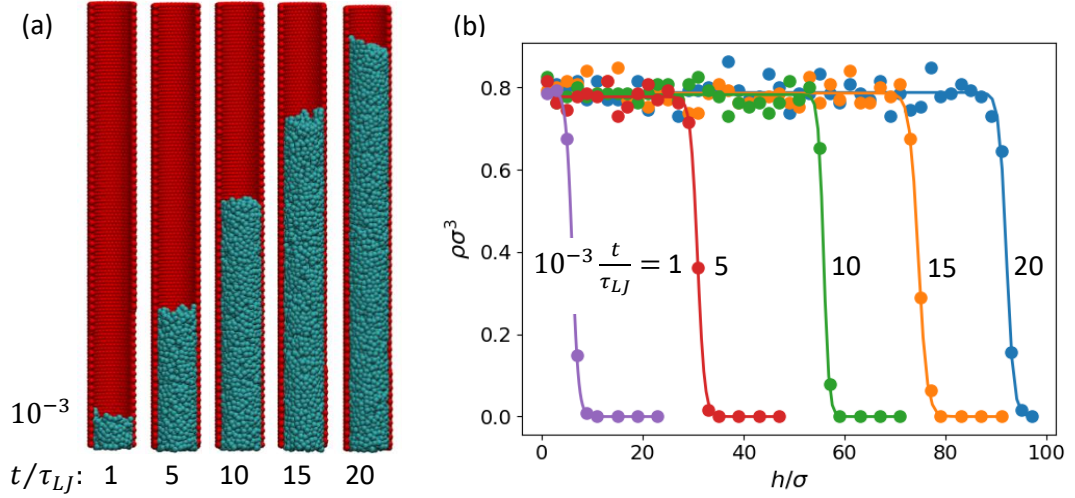


Figure 3.3: (a) A cylindrical capillary with diameter $D = 9$, height $H = 100$, and polymer chains of length $N = 10$ are used to simulate the process of polymer wicking. At $10^{-3} t/\tau_{LJ} = 1$, the polymers are held outside the capillary by unfavorable interactions but can still fluctuate as a free surface at the mouth of the capillary. For $t > 0$, the interactions between capillary and polymers are turned up to induce wicking into the capillary. (b) the height of the polymer interface can be tracked by fitting a sigmoidal function to $\rho(z)$. The full system showing the polymer film beneath the pore is shown in Supplemental Information.

The height of the melt in the capillary is calculated by fitting $\rho(z) = \frac{\rho_l + \rho_v}{2} - \frac{\rho_l - \rho_v}{2} \tanh\left[\frac{2(z - z_0)}{l}\right]$ to the density profile, as shown in Figure 3.3b, where ρ_l is the density of the polymer melt in the capillary, ρ_v is the density of vapor in the capillary, z_0 is the height of the interface, and l is the thickness of the interface. The polymer-vapor interface has a thickness of $1 - 2\sigma$. Due to low polymer vapor pressure, $\rho_v = 0$ for all but the shortest chains. The polymer height (h) is roughly proportional to time (t) as shown in Figure 3.4, which is consistent with the inertial regime of capillary imbibition.[31]

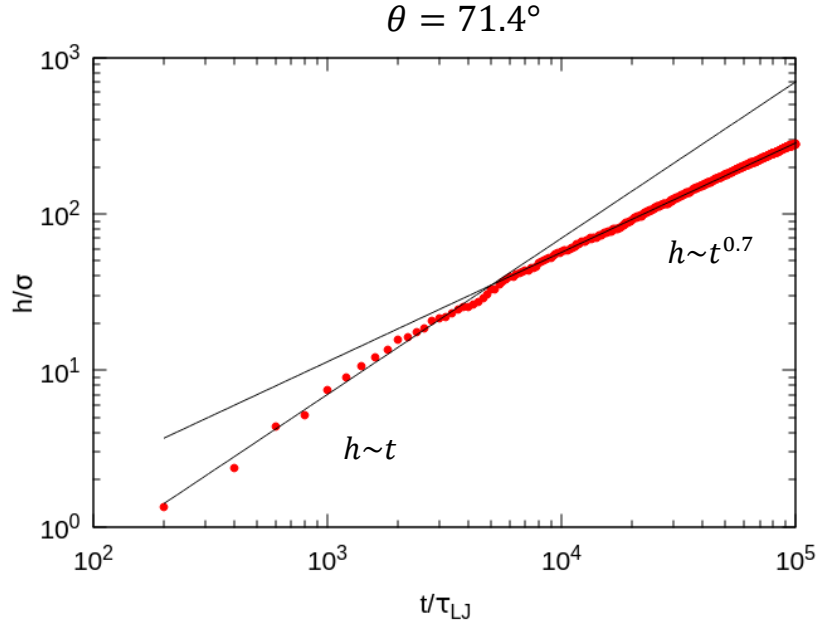


Figure 3.4: Infiltration height as a function of time. The scaling at early times is consistent with the inertial regime, while the scaling at later times appears to approach the Lucas-Washburn (LW) scaling.

My focus is to identify the critical angle above which infiltration of polymers into nanopores ceases to occur. Thus, I run each simulation for at least a diffusion time, $t/\tau_{LJ} = R_e^2/\mathcal{D}$ where \mathcal{D} is the bulk diffusivity of a polymer of length N and $\tau_{LJ} = \sigma\sqrt{m/\varepsilon}$ where τ_{LJ} is the LJ timescale calculated from LJ parameters ε and σ , and the mass, m . On these timescales, the polymers in the film below the capillary are able to relax sufficiently that I expect my simulations to not be limited by kinetic traps. As discussed below, conclusions based on this protocol agree with conclusions drawn from the free energy change during infiltration.

3.3 Correlating contact angle with interatomic interactions

The strength of interactions between a solid surface and a liquid at the macroscopic scale is often expressed in terms of contact angle, θ , which in my model is primarily controlled through the LJ parameter ε_{PC} . To correlate these two parameters, I determine the contact angle of a polymer droplet with a pseudo-infinite cylindrical geometry[51] on the solid surface with the same lattice structure as the cylindrical pores as shown in the inset of Figure 3.5a. The use of cylindrical geometry removes the curvature of the contact line so that the contact angle determination is not affected by line tension and in turn remains independent of the size of the sessile drop. All simulations start with a melt droplet contact angle close to 90° and are annealed until the contact angle reaches a constant value.

I observe two prominent trends in the contact angle shown in Figure 3.5a. First, $\cos \theta$ is proportional to ε_{PC} for all chain lengths, N , which is expected as stronger enthalpic interactions between polymer chains and the solid surface will induce stronger wetting (i.e., smaller θ). Interestingly, for a given value of ε_{PC} , θ increases ($\cos \theta$ decreases) for increasing N .

As the physical reason behind the observed dependence of polymer contact angle on N for a given ε_{PC} is not obvious, I further investigate the role of the interfacial tension of the free polymer surface in dictating the contact angle. I calculate the surface tension from the asymmetry of the pressure tensor in a free-standing, planar thin film simulation.[19], [52] It is known from previous work on the concentration of chain ends at free interfaces that the surface tension can depend on chain length and saturates for long chains.[53], [54] It was previously reported that the segregation of the chain ends to interfaces leads to this

entropic contribution to the surface tension, and the dependence of the interfacial tension on N has a form that does not depend on the details of the molecular model.[55]

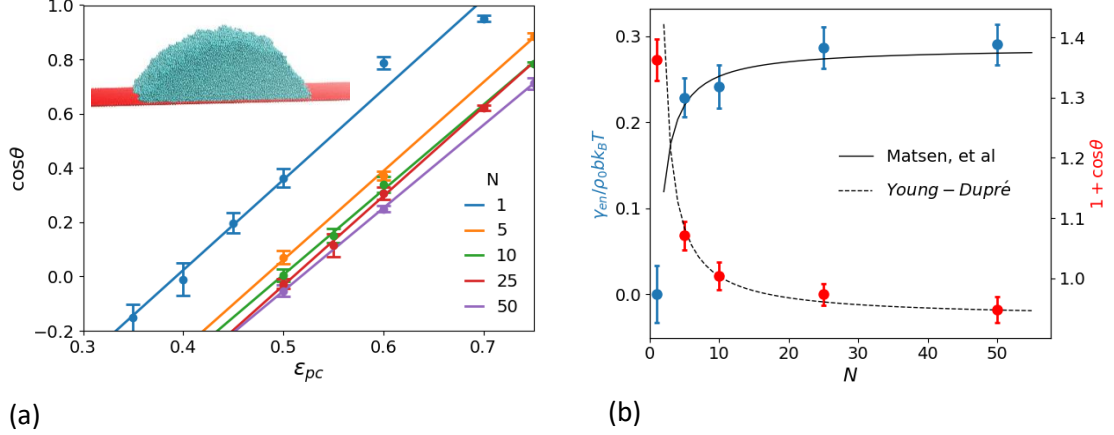


Figure 3.5: (a) Contact angle simulations are used to parameterize the relationship between the interaction energy (ϵ_{pc}) and contact angle (θ). ϵ_{pc} varies approximately linearly with $\cos \theta$ for all values of N . (b) The dependence on chain length N is explained by the molecular weight dependence of the surface tension (γ) from Ref [55] and the work of adhesion from the Young-Dupré equation for $\epsilon_{pc} = 0.5$. The work of adhesion measured is $W_{ad} = 0.155 \epsilon/\sigma^2$. Literature[56] reports similar values for LJ polymers.

This entropic component of surface tension, γ_{en} , when added to the simple fluid surface tension, γ_1 , yields the total surface tension, γ . Thus, I plot surface tensions in Figure 3.5b from simulation by first computing $\gamma - \gamma_1$ with the simulated values, where γ_1 was calculated for a film of a simple LJ fluid. I expect this quantity to be comparable to the theoretical γ_{en} presented in Ref. [55] and is given as

$$\frac{\gamma - \gamma_1}{b\rho_0 k_B T} \approx \frac{\gamma_{en}}{b\rho_0 k_B T} = \Gamma_\infty - \frac{2A}{N}, \quad 3.1$$

where Γ_∞ and A are constants previously computed from self-consistent field theory[55] for polymers with Hookean spring bonds; they can be interpreted as the surface tension of infinitely long polymers and the contribution from a single chain end, respectively. The other constants b , ρ_0 , and $k_B T$ are the Kuhn length, monomer density, and temperature,

respectively, which are each measured for my system. I observe in Figure 3.5b that the entropic component of my surface tension is in good agreement with Eq 3.1, even though I use the parameters Γ_∞ and A taken from the calculations in Ref [55].

Rearranging and inserting Eq 3.1 into the Young-Dupré equation provides an expression for the N dependence of the contact angle,

$$1 + \cos \theta \approx \frac{W_{ad}}{\gamma_1 + \gamma_{en}} = \frac{W_{ad}}{\gamma_1 + b\rho_0 k_B T \left(\Gamma_\infty - \frac{2A}{N} \right)} \quad 3.2$$

where W_{ad} is the work of adhesion between the polymer and surface[57] as defined by $W_{ad} = \gamma_C + \gamma - \gamma_{PC}$. Fitting Eq 3.2 to the contact angle data in Figure 3.5 by varying W_{ad} at $\varepsilon_{PC} = 0.5$ gives $W_{ad} = 0.155$, which is in good agreement with previous simulation studies[56] of similar polymer models. This consistency suggests that chain ends influence the contact angle and that the saturation of the contact angle results from a reduction in the number of chains at the solid-polymer interface and free surface. However, the work of adhesion remains nearly constant due to a balance between γ and γ_{PC} , as can be seen in the definition of W_{ad} .

3.4 Computing Critical Contact Angle from Dynamics

I probe the effect of confinement on infiltration of polymer chains into nanopores by varying both the chain length and capillary diameter and determining the critical contact angle for infiltration to occur by varying the interactions of the polymer with the capillary walls, ε_{PC} . The extent of confinement is quantified with a confinement ratio $\delta = \frac{R_e^2}{D^2}$ where D is capillary diameter. To distinguish whether a particular set of conditions leads to spontaneous infiltration of the polymers, I expect that the melt should infiltrate to a height

larger than the polymer's end-to-end distance within a diffusion time, $\tau_e \sim R_e^2/D$. When the height inside the capillary increases at such a rate, I interpret the results as implying that any observed infiltration is driven by polymer-surface interactions and not governed by a diffusion process. For example, in Figure 3.6 I plot the infiltrated height of $N = 50$ polymer infiltrating a pore of $D = 5$ as a function of time; I observe that only for a contact angle $\theta \leq 82^\circ$, infiltration is observed.

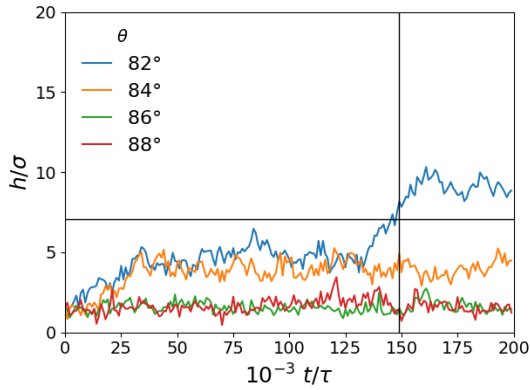


Figure 3.6: Height trajectories of flexible polymer chains of length $N = 50$ show that the polymers only infiltrate past their mean squared end-to-end distance (black line) if $\theta < 84^\circ$. The pore diameter D is 5σ .

In Figure 3.7a, I show the calculated critical contact angles by identifying chains that undergo infiltration under varying pore and chain sizes. For flexible chains, I observe a suppression of the critical contact angle from the simple fluid to small N . However, θ_c reaches a plateau at approximately 83° and does not show an observable dependence on N for $N \geq 25$. Given that the entropy of an ideal chain scales with chain length, $\Delta S \sim R_e^2 \sim N$, and that confinement causes a loss of entropy proportional to N , [38] it is initially surprising that θ_c does not depend on N for large N or strong confinement as shown in Figure 3.7b. To verify my empirical definition of θ_c , I have calculated the free energy of infiltration using umbrella sampling for select values of N . The umbrellas are implemented

by biasing the separation between centers of mass between the surface containing the capillary and the polymer melt with a harmonic potential. The critical contact angle determined based on free energy calculations for three values of N (Figure 3.7a and b) show little dependence on N and are slightly larger than plateau I obtained based on the diffusion length criteria. The small difference in θ_c obtained using the two approaches I believe may be due to an entrance effect near the base of the capillary.

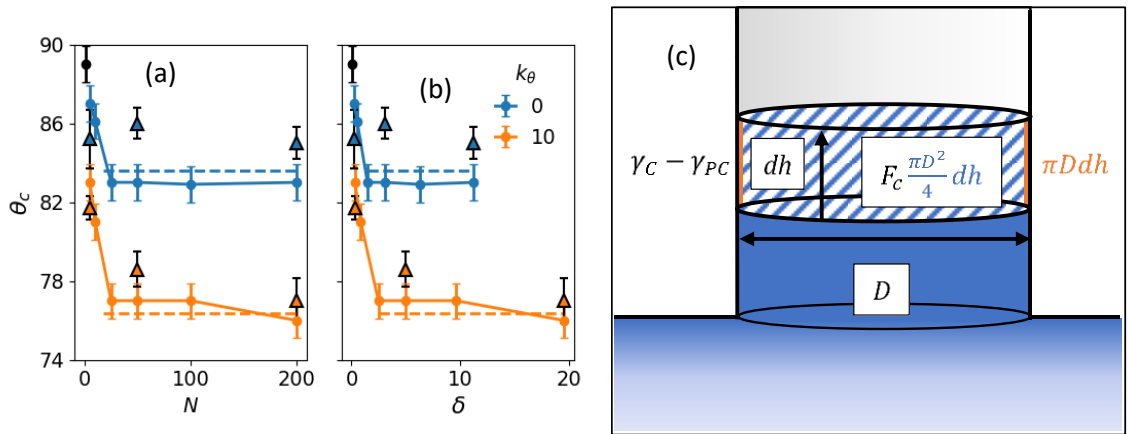


Figure 3.7: (a) Critical contact angle versus chain length, N , and (b) degree of confinement, δ . The critical angle for infiltration of flexible chains plateaus around a value of 83° whereas the critical value for stiff chains plateaus around 77° . The dashed lines indicate theoretical predictions from the energy balance. (c) Diagram showing how change in height, dh , relates to pore geometry and free energy.

3.5 Computing Critical Contact Angle using Umbrella Sampling

Umbrella sampling is often used in free energy calculations to facilitate the calculation of the free energy along a reaction coordinate in a system. In my system, the desired free energy is the free energy change as the height of the polymer in the capillary increases; since I am only interested in the sign of the derivative as the polymer height increases, I do not need to know the absolute free energies. I employ an umbrella potential $U_{umb}(z) =$

$\frac{K}{2}(z - z_0)^2$ where K is the potential strength and z is the center of mass separation of the polymer melt and the rigid body containing the capillary. This potential holds the infiltrating fluid at a height inside the capillary by constraining the center of mass separation to z_0 . By varying z_0 , I can reconstruct the free energy gradient experienced by the polymer fluid for different contact angles as it infiltrates and observe when the gradient changes sign (i.e., from negative (infiltrating) to positive (non-infiltrating)).

I compute the biased potential of mean force from $-kT \ln P(z)$ where $P(z)$ is the probability distribution of center of mass separations. The bias is then removed to give the actual relative free energy $w(z) = -kT \ln P(z) - U_{umb}(z)$. Sample plots of $z(t) - z_0$, $-kT \ln P(z - z_0)$, and $w(z)$ are shown in Figure 3.8. Addition of a constant to free energy curves calculated at different values of z_0 (infiltration heights) can be used to reconstruct the full free energy curve as shown in Figure 3.8a. I calculate the slope of the free energy curves for several values of z_0 and use the variation in the slope as an estimate for the error. Plotting slope versus θ in Figure 3.9b allows us to graphically show the location of the critical value from the free energy gradient.

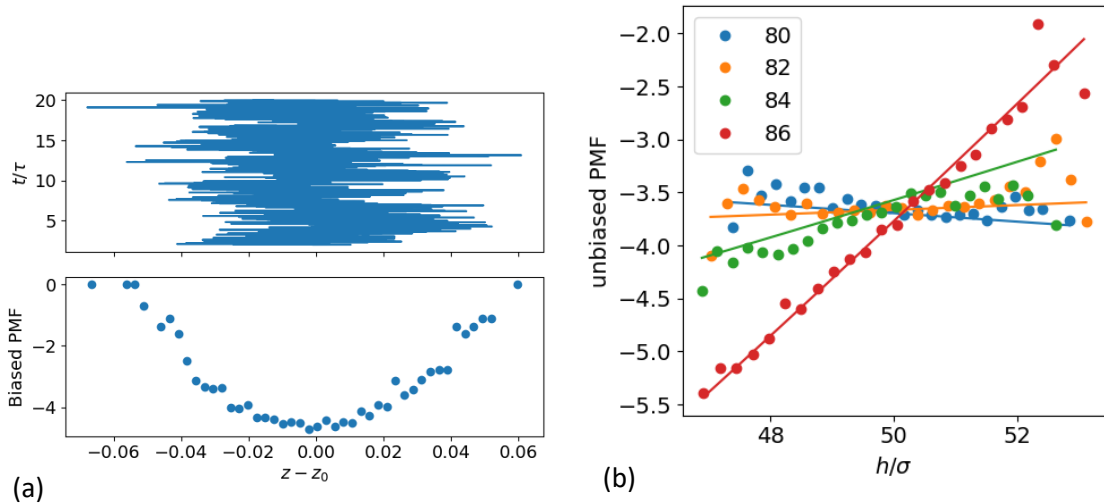


Figure 3.8: (a) The biased potential of mean force is computed from the probability distribution of $z - z_0$ produced by the umbrella sampling simulations. (b) Subtracting the biasing potential from the PMF provides free energy curves with unknown additive constant.

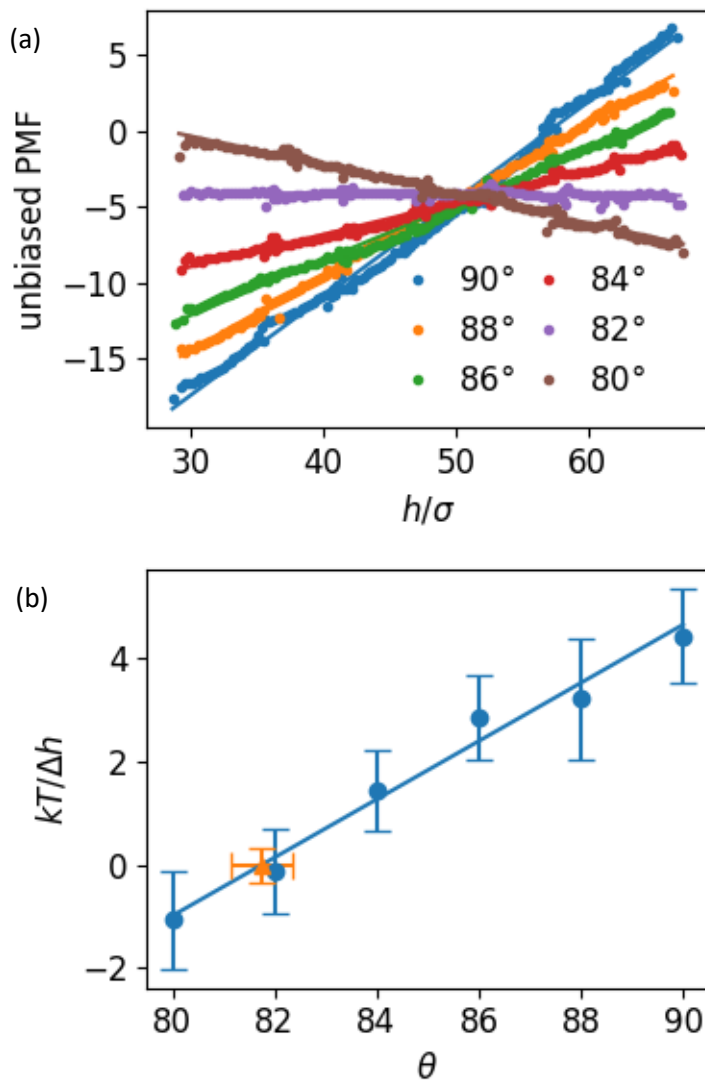


Figure 3.9: (a) Specifying the offsets for free energy curves manually allows us to roughly reconstruct the full free energy curves. I observe that for the 6 different contact angles the slope of the free energy switches signs. (b) Fitting a line to the slopes of the free energy curves vs contact angle allows us compute the critical contact angle ($\approx 82^\circ$). Error bars are computed from replicates and multiple sampling windows.

The center of mass coordinate, z , was converted into a height coordinate, h , using the expression

$$h = \frac{A\delta_0}{A_c - A} \left(1 - \sqrt{1 - \frac{A_c - A}{A_c} \left[1 - \frac{2z}{\delta_0} + \frac{A_s}{A - A_c + A_s} \frac{H}{\delta_0} \right]} \right) \quad 3.3$$

where A is the area of the polymer film, A_c is the cross-sectional area of the capillary, A_s is the surface area of the capillary, δ_0 is the initial thickness of the polymer film, and H is the full height of the capillary.

3.6 Deriving the Free Energy Model

To understand this trend, I develop a free energy model accounting for contributions from surface free energy and the confinement free energy[38] similar to the model presented recently.[48] As shown schematically in Figure 3.7c, the change in surface area with a change in height dh is $dA = \pi D dh$ and thus the gain in surface energy can be expressed as $(\gamma_C - \gamma_{PC})dA$ where γ_C is the capillary surface energy and γ_{PC} is the polymer-capillary interfacial energy. The differential change in the confinement free energy as the fluid height increases can be expressed by taking into account the loss of conformational entropy $k_B T \left(\frac{N b^2}{D^2} \right) \rho dV$, where $\rho = \rho_0/N$ is the density of polymer chains, and $dV = \frac{\pi D^2}{4} dh$ is the increase in volume of the polymer in the cylindrical tube. Combining the entropic penalty with the contributions from the interfacial tension, the total change in the free energy upon a change in height dh is the sum of these two contributions, which gives

$$dF = (\gamma_C - \gamma_{PC})\pi D dh + kT \left(\frac{N b^2}{D^2} \right) \rho \frac{\pi D^2}{4} dh. \quad 3.4$$

By substituting in Young's equation[57], $\cos \theta = (\gamma_{PC} - \gamma_C)/\gamma$, converting the chain density, ρ , to the monomer density, $\rho_0 = \rho N$, and setting the free energy change $dF/dh = 0$, an analytical solution for the critical contact angle can be obtained as

$$\cos \theta_c = \frac{\rho_0 k T b^2}{4\gamma D}. \quad 3.5$$

Remarkably, Eq. 3.5 suggests that the critical contact angle does not depend on N , consistent with my simulations results for $N > 25$. This result can be rationalized by considering the competing effects of chain entropy and the number of chains in the cylindrical pore. Although increasing the confinement of a single chain results in a loss of entropy, this change is compensated by the number of chains confined in the cylindrical pore such that the total melt entropy remains constant. Eq. 3.5 also predicts that critical contact angle should depend on Kuhn length, b , such that a polymer with a larger Kuhn length would result in smaller θ_c .

To test this prediction, I perform infiltration simulations with a semi-flexible model polymer that has a larger Kuhn length, which are produced by adding the angle potential $u(\theta) = \frac{k}{2} \left(\theta - \frac{2\pi}{3} \right)^2$ along the backbone of the polymer chain.[50] Calculating the persistence length from the decay of the bond-autocorrelation function, I show that these semi-flexible chains with $b \approx 2l_p \approx 2.62\sigma$ are stiffer than the flexible chains where $b \approx 1.24\sigma$.

The critical contact angles calculated for these semi-flexible chains using the kinetic and the umbrella sampling approaches are also shown in Figure 3.7a. As was the case with the flexible chain, the critical contact angle shows a reduction up to $N \approx 25$ and then plateaus around 77° , lower than that of the flexible chains.

I can analytically predict the value of the plateau in $\cos \theta_c$ by substituting Eq 3.1 into Eq 3.5 and taking the limit for large N to find

$$\cos \theta_c = \frac{b/D}{4 \left(\frac{\gamma_1}{\rho_0 b k_B T} + \Gamma_\infty \left(1 - \frac{2A}{\Gamma_\infty N} \right) \right)} \approx \frac{b/D}{4(\Gamma_1 + \Gamma_\infty)} \quad 3.6$$

where $\Gamma_1 = \frac{\gamma_1}{\rho_0 b k_B T}$. I observe from Eq 3.6 that dimensionless surface tensions for both simple fluid (Γ_1) and infinite chains (Γ_∞) and the ratio b/D are sufficient to characterize θ_c in the long-chain limit. Since the monomeric fluid has the same dimensionless surface tension Γ_1 for both polymer models, and if I assume Γ_∞ is insensitive to small changes in the backbone stiffness, then the changes in b accounts for the plateaus of 83° and 77° observed in θ_c in Figure 3.7a and b. Thus, the more rigid polymer backbones decrease the critical contact angle for infiltration more than a flexible polymer backbone.

3.7 Critical contact angle of polymer infiltration into nanoparticle packings

Although I observe a depression of the critical contact angle in cylinders that is independent of chain length for long chains, I wish to know whether these results extend to infiltration in nanoparticle packings. Due to the large size of the packings, umbrella sampling becomes significantly slower and more expensive due to the large number of simulations and high degree of parallelism required to perform it efficiently. Therefore, I rely on dynamic profiles of infiltration to determine the critical contact angle.

Using chains with length $N = 1, 5, 10, 25,$ and 50 , I calculated their critical contact angles in the nanoparticle packing by infiltrating them into the same packings from Chapter 2.2 at different contact angles. The height was calculated following the

integration protocol in Chapter 2.3 with a cut-off fraction of 99% of the total monomers. A plot of height vs time for a simple fluid ($N=1$) is shown in Figure 3.10 for different contact angles. It is not immediately apparent which curves are infiltrating or not near the critical angle, since the height changes slowly with time. To make visualization easier, the profiles of height versus time, such as those shown in Figure 3.10a, are converted into profiles of height versus contact angle, as shown in Figure 3.10b, by plotting profiles at select time points. As contact angle increases in these plots, the height profiles converge together, indicating that there is less infiltration. We can extract a qualitative estimate of the critical value from these plots by looking at the contact angle where the height curves appear to converge. In the simple fluid case ($N = 1$) shown in Figure 3.10a and b, contact angles higher than 90° provide a visual baseline for the variance in the height that can be used to determine whether infiltration is occurring.

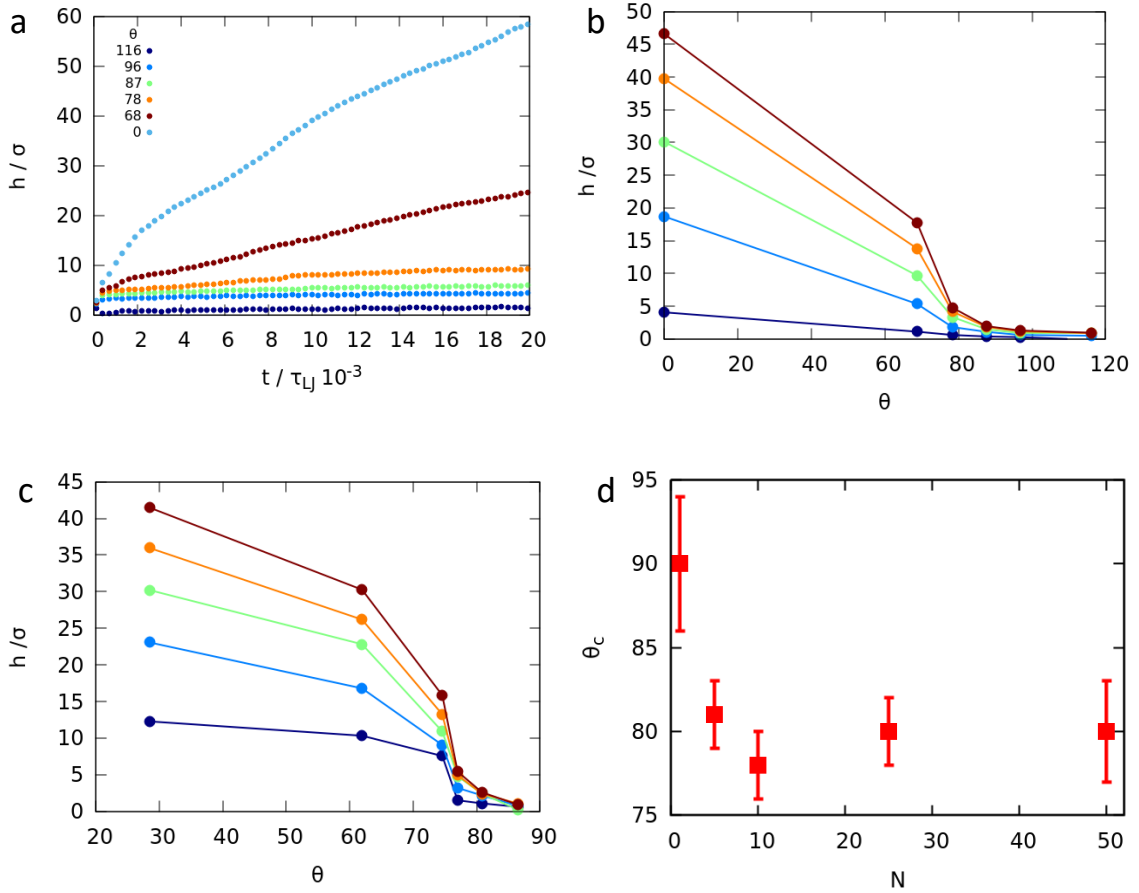


Figure 3.10: (a) Simple fluid infiltration h vs t (b) Simple fluid h vs θ for select time points showing that infiltration appears to stop at 90° . (c) $N=5$ infiltration h vs θ for select time points. Infiltration appears to stop just above 80° . (d) Critical contact angle values for different chain lengths.

In Figure 3.10c, I show a sample set of curves for $N=5$ to illustrate how these curves appear for a polymer. Although I did not perform infiltration for polymers above a contact angle of 90° , the polymers should have a very similar baseline to the simple fluid case. Visually comparing to the baseline in Figure 3.10b, it appears that the critical contact angle is around 80° . We can approximate the error in the critical contact angle using the distance between the critical contact angle and the surrounding contact angles used for other infiltration trajectories. After extracting the critical contact angle for each system, I observe in Figure 3.10d that they also have a plateau as observed in the

cylindrical capillaries. Since this is a less precise method for extracting the critical contact angle, the plateau is at a lower value than observed in cylindrical capillaries.

3.8 Summary

In this work, I have shown that despite the confinement-induced loss of entropy that is experienced by individual polymer chains, the critical contact angle that induces spontaneous surface-driven infiltration of polymers into cylindrical pores does not strongly depend on N , for large N . The stiffness of the chain, as represented in terms of the Kuhn segment length, rather than the overall length of the chain determines the critical contact angle. The implications of these findings are that stiffer chains in a melt have a smaller window of contact angles under which they can infiltrate narrow pores. Additionally, studying model cylinder geometries provides insight for polymer imbibition into other porous media such as random packings of nanoparticles, which have paved the way towards new fabrication methods of composite materials with extremely high volume fractions of nanoparticles.[4] However, nanoparticle packings have many features that are not present in cylinders, including a cross-section that varies with height. The presence of expansions and constrictions in the cross-section could introduce large barriers into the free energy due to the change in the free surface area. Thus, it would be useful to study capillaries that share these structural features with nanoparticle packings.

CHAPTER 4: Infiltration of polymer into nano-capillaries with periodically varying cross-section

4.1 Introduction

Capillary infiltration is typically modeled with the Lucas-Washburn equation. As explained in Chapter 1.3, the Lucas-Washburn equation is derived for cylindrical geometries and adapted to packings using empirical correction factors. Despite the success of this simple model, it would be useful to investigate whether other geometries could provide insight into other features relevant to different porous media. A feature of nanoparticle packings not captured by cylinders is the changing cross-section with height and variation in pore size. As described in Chapter 2.3, regions with necking can be very important to the final distribution of polymers in undersaturated systems; however, small necks could potentially provide physical barriers for infiltration to occur.

An interesting alternative geometry to explore is a capillary with sinusoidally varying diameter. This geometry retains the smooth, continuous features of a cylinder while also capturing the periodic constrictions of a nanoparticle packing and excluding tortuosity and pore connectivity. Prior work on these capillaries of non-constant cross-section has almost exclusively focused on macroscale problems using continuum theory, such as the derivation in Chapter 1.3. However, in nanoparticle packings, confinement and non-continuum mechanics could be important to understanding the infiltration behavior of polymers. Additionally, only one study attempts to connect free energy to infiltration behavior in these wavy capillaries, but doesn't verify the validity of the free energy they

compute[37]. Figure 4.1 shows the power consumption, free energy, tube radius, infiltration resistance, and curvature of the capillary in question.

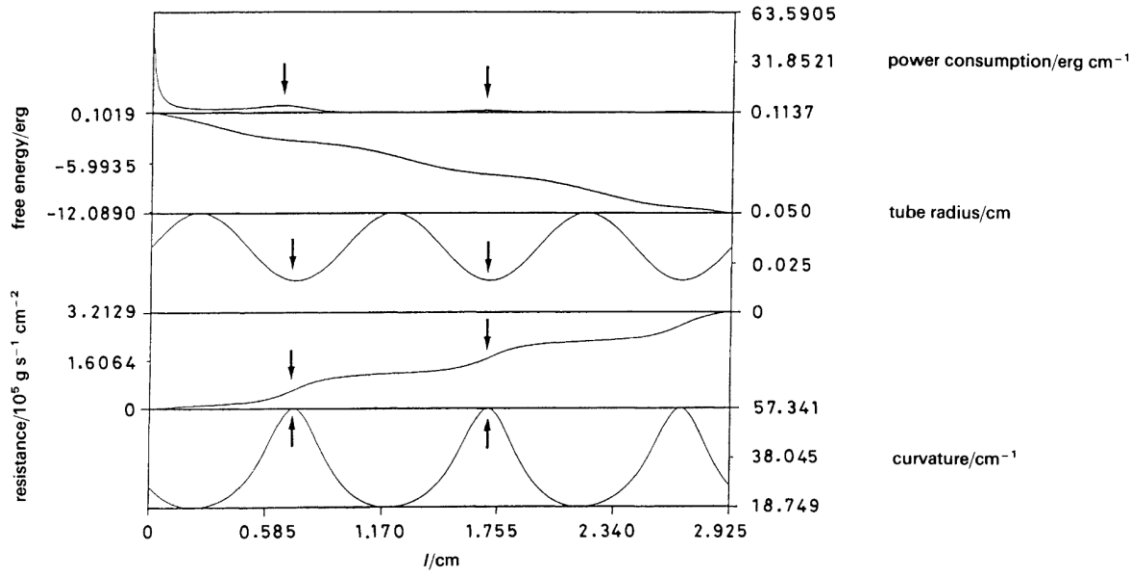


Figure 4.1: Variation of meniscus curvature, resistance to liquid flow, tube radius, free energy as the liquid penetrates the tube and the accompanying power consumption by the liquid during penetration are plotted as a function of position in the sinusoidal tube. At the constrictions, marked by an arrow, the curvature of the meniscus, resistance to flow and power consumption increase. The free energy decreases monotonically as penetration proceeds. These calculations were for silicone oil ($\eta = 971$ cP, $\gamma = 21.2$ dyn cm^{-1} , $\theta = 20^\circ$)[37].

Finally, wavy capillaries with low wave amplitudes are favored in these studies because the meniscus cannot satisfy the contact angle without intersecting the wall at multiple points in continuum mechanics studies. However, infiltration into packings of very high aspect ratio particles would include pores with wave amplitudes well above those studied previously. Additionally, no one has yet applied molecular dynamics simulations to studying capillaries with sinusoidally varying cross-section. Molecular dynamics has the

advantage of simulating polymer confinement and the infiltrating meniscus directly at the molecular scale rather than relying on assumptions from continuum theory.

Therefore, the goal of this chapter is to understand the influence of necks and voids in capillaries with sinusoidal walls and exploring the connection between the local free energy landscape and infiltration dynamics. I will use umbrella sampling combined with infiltration studies to map out the free energy as a function of height and determine how the infiltration height is affected, and the results will be compared to analytic continuum models.

4.2 Making Wavy Capillaries

Wavy capillaries are generated using a sinusoidal function $D(h) = D_0 + 2A_0 \cos\left(\frac{2\pi h}{\lambda} + \phi\right)$ where D_0 is the average or “cylinder” diameter of the capillary, A_0 is the amplitude of the wall variation, h is the height along the axis of the capillary, λ is the wavelength of the sinusoid, and ϕ is a shift factor that changes whether the mouth of the capillary is a void or neck. Capillaries are constructed with unit area per site of 0.717, which is similar to the surfaces of the plates, cylinders and particles in my previous studies. Figure 4.2a shows an example capillary to illustrate. I do not account for the curvature of the free surface in the following calculations. This is partially to simplify the calculation so that an analytical model can be derived but is also found to agree well with the simulated free energy curves. Additionally, due to the high wave amplitudes in the capillaries, a spherical meniscus cannot satisfy both the contact angle and capillary boundaries.

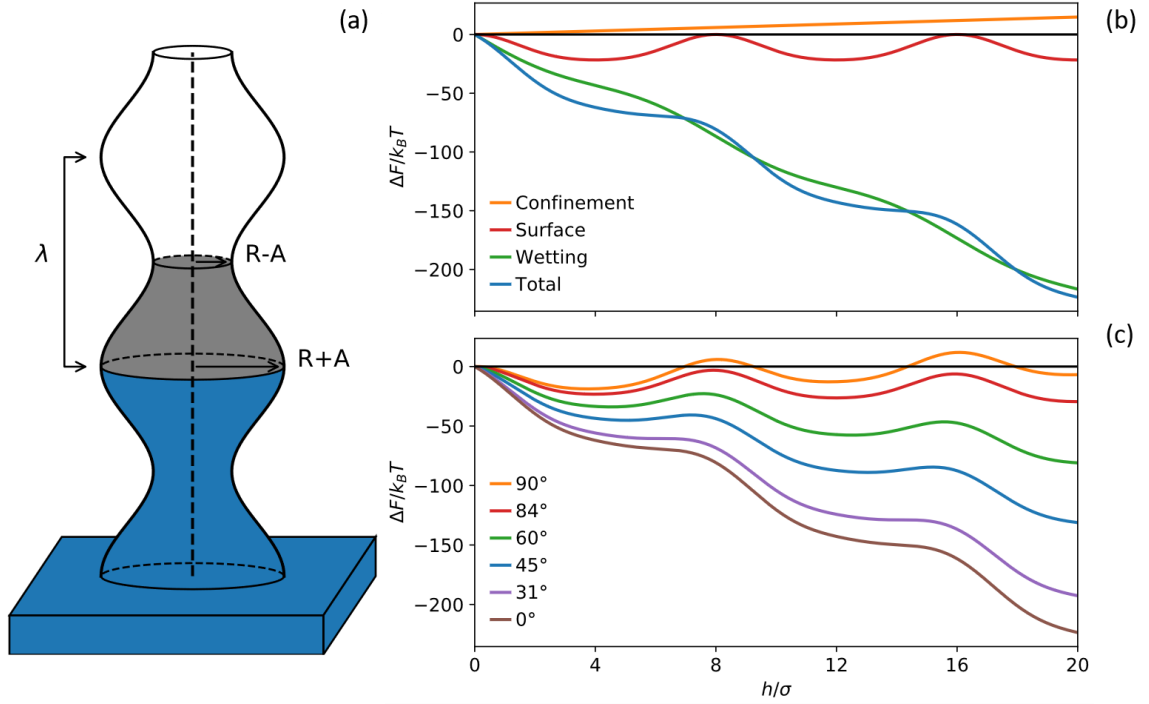


Figure 4.2: (a) A wavy capillary is characterized by its amplitude, A , radius, R , and wavelength, λ . (b) The free energy in a wavy capillary has 3 main contributions: polymer confinement (orange), free surface expansion and contraction (red), and wetting (green). (c) By changing the relative importance of each term, barriers can be introduced into the free energy profiles. Increasing the contact angle, θ , reduces the role of wetting and halts infiltration.

4.3 Derivation of the Free Energy Model

The volume of a wavy capillary is calculated as

$$V = \pi h \left(\frac{D_0^2}{4} + \frac{A_0^2}{2} \right) + \frac{\lambda A_0 D_0}{2} \sin \left(\frac{2\pi h}{\lambda} \right) + \frac{\lambda A_0^2}{8} \sin \left(\frac{4\pi h}{\lambda} \right) \quad 4.1$$

When compared to a cylinder with similar diameter, the volume is observed to increase faster on average in the wavy capillary than the cylinder. Scaling the volume by D^2 and λ (a cylinder with same average volume and height equal to a single period) shows that two main groups emerge, $W = \frac{A_0}{D_0}$ and $H = \frac{2\pi h}{\lambda}$. The first group W indicates how wavy the capillary is and the second indicates the fluid height relative to constriction/expansion locations.

The free energy can be derived by considering the free energy of confinement, wetting, and free surface. For a given change in height, the volume changes as $dV = \frac{\pi D^2(h)}{4} dh$, the wetted perimeter changes as $dA = \pi D(h) dh$, and the free surface area (i.e. the capillary cross-section) changes as $dA = \frac{\pi D}{2} \left(\frac{dD}{dh} \right) dh$. Using the de Gennes confinement free energy for a chain in a melt, the free energy gradient can be written as

$$dF = \rho_0 k_B T \left(\frac{b}{D} \right)^2 \frac{\pi D^2}{4} dh - \gamma_p \cos \theta \pi D(h) dh + \gamma_p \frac{\pi D}{2} \left(\frac{dD}{dh} \right) dh. \quad 4.2$$

Integrating along the height of the capillary gives

$$\begin{aligned} \Delta F = & \frac{\pi}{4} \rho_0 k_B T b^2 h - \pi D_0 \gamma_p \cos \theta h - \lambda A_0 \gamma_p \cos \theta \left[\sin \left(\frac{2\pi h}{\lambda} + \phi \right) - \sin \phi \right] \\ & + \pi A_0 D_0 \gamma_p \left[\cos \left(\frac{2\pi h}{\lambda} + \phi \right) - \cos \phi \right] \\ & + \pi \frac{A_0^2}{2} \gamma_p \left[\cos \left(\frac{4\pi h}{\lambda} + 2\phi \right) - \cos 2\phi \right] \end{aligned} \quad 4.3$$

Since the infiltrating driving force is proportional to $\cos \theta$, I expect that changing θ will lead to regimes where there are appreciable barriers along the capillary. This is predicted in Figure 4.2 showing the effect of changing θ on free energy.

Observe that H appears in the free energy and that scaling by $D\lambda$ produces W and 2 other groups. The scaled equation becomes

$$\mathcal{F} = \frac{BH}{8} - \Gamma_p \cos \theta \left[\frac{H}{2} + W\Delta \sin(H + \phi) \right] + \frac{G\Gamma_p}{2} \left[\Delta \cos(H + \phi) + \frac{W}{2} \Delta \cos(2H + 2\phi) \right] \quad 4.4$$

with the groups $\mathcal{F} = \frac{\Delta F}{\rho_0 k_B T b D_0 \lambda}$, $B = \frac{b}{D}$, $\Gamma_p = \frac{\gamma_p}{\rho_0 k_B T b}$, $G = \frac{2\pi A_0}{\lambda}$. The group G is an estimate of the maximum slope of the capillary wall, which indicates how rapidly the cross-section changes. Plotting the free energy in Figure 4.3: for high G (a) and low G (b) shows that G can dictate whether the necks and avoids create periodic barriers in the capillary.

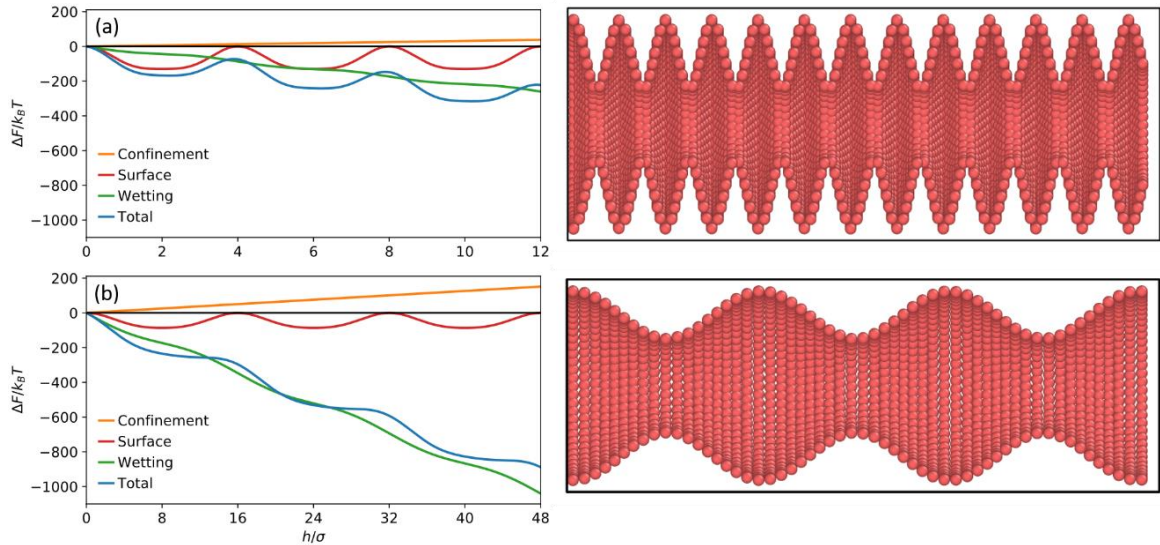


Figure 4.3: $\lambda = 4$, $A_0 = 3$ has rapidly changing cross-section and barriers exceeding $k_B T$ by $\sim 10^2$. (b) $\lambda = 16$, $A_0 = 2$ has a slowly changing cross-section with no barriers in the total free energy. Changing the geometric parameters of the wall, I can artificially create energy barriers even under highly wetting conditions. Thus, some highly wavy walls would be resistant to infiltration of most imbibing fluids.

4.4 INDirect Umbrella Sampling

As explained in Chapter 3.5, umbrella sampling is a free energy computation method that uses biasing potentials to improve sampling in particular regions of phase space. Whereas sampling infiltration free energies in cylinders was performed by controlling the center of mass separation between the cylinder and the polymer melt, this method of umbrella sampling was determined to not be sensitive enough to capture the features of the free energy model for the wavy capillaries. Therefore, I turned to a technique called INDirect Umbrella Sampling (INDUS). INDUS computes the probability that a number of atoms, N , are found in a probe volume. It was originally developed as a means to study water thermodynamics, wetting, and the free energy of hydration around proteins[58]–[60]. The biasing potential is computed as $(N) = \frac{\kappa}{2} (\tilde{N} - N^*)^2$, where κ is the strength of the biasing potential, N^* is the window center, and \tilde{N} is a field that is closely correlated to the number of atoms found in the probe. This field smears the interaction between particles, \mathbf{r}_i , and the boundary of the probe volume, v , and is computed over all atoms, M ,

$$\tilde{N} = \sum_{i=1}^M \int_v \Phi(\mathbf{r} - \mathbf{r}_i) d\mathbf{r} \quad 4.5$$

where $\Phi(\mathbf{r} - \mathbf{r}_i) = \phi(x)\phi(y)\phi(z)$ and $\phi(\alpha) \propto [e^{-\alpha^2/2\sigma^2} - e^{-\alpha_c^2/2\sigma^2}]\Theta(\alpha_c - |\alpha|)$.

Thus, as particles approach the boundary of the probe volume, they contribute to the overall number of particles in the probe volume to give a continuous bias potential. Also, since the smearing function $\phi(\alpha)$ is cut-off at α_c forces are only applied on particles that are close to the boundary, rather than the entire set of particles.

I use a cylindrical probe volume with diameter $D_0 + 2A_0$ and with base at -1 and stretching the entire length of the capillary to sample the number of monomers within a wavy capillary. Since the capillary starts at $h = 0$, the probe volume extends a short way into the melt to allow sampling of the free energy for the interface relaxation as well as the start of infiltration. I would expect that this interface collapse is roughly quadratic with height since the interface forms a spherical cap.

After sampling the free energy as a function of the number of monomers in a capillary, I can convert N to h by fitting $\rho_0 V(h)$ to data from all the umbrella windows. Finally, all the umbrella windows are stitched together using the Weighted Histogram Analysis Method (WHAM) [58], [61]–[63] equations

$$e^{-\beta f_k} = C \sum_{j=1}^{n_w} \sum_{l=1}^{n_j} \frac{e^{-\beta U_k(\tilde{N}_{jl})}}{\sum_{i=1}^{n_w} n_i e^{-\beta [U_i(\tilde{N}_{jl}) - f_i]}} \quad 4.6$$

where $\{f_k\}$ is the set of free energy offsets, U_k is the bias potential, and the double sum runs over each of the total n_w windows and over all the bins n_j in the j th window, respectively. The constant C is a normalization constant for the total histogram. This method reweights the distributions from each window by minimizing the overlap error between the distribution tails. This is identical to applying a vertical shift to the potential of mean force in each window so that a continuous free energy curve is produced.

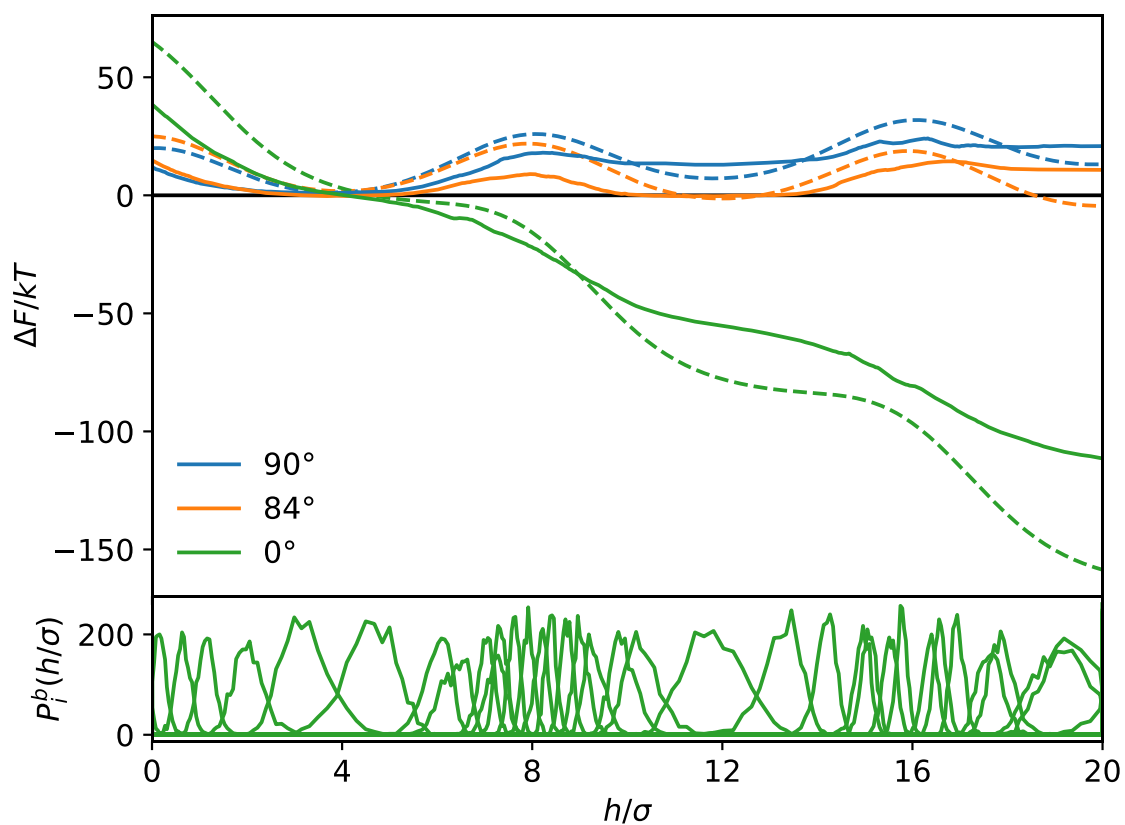
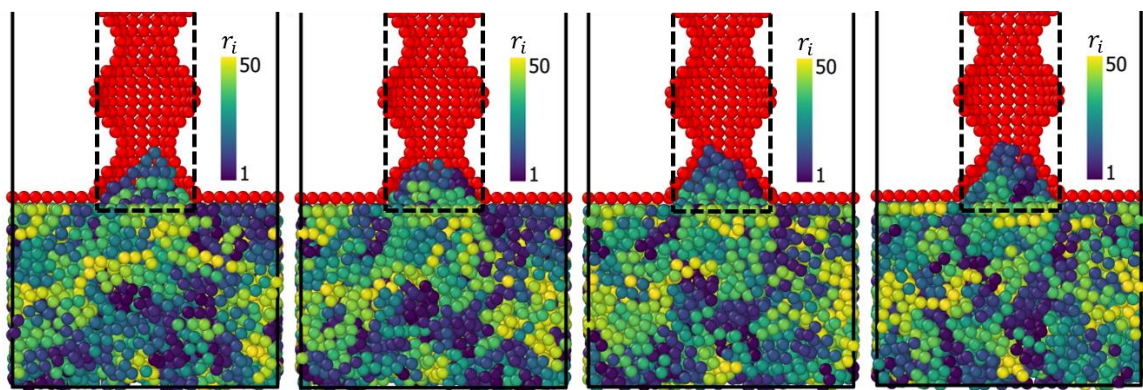


Figure 4.4: Free energy from theory predicts the presence of local minima and maxima that can vanish above a certain contact angle. The same is observed in simulations for the contact angles of 0° , 84° , and 90° , however, the free energy barriers are lower than predicted.

Figure 4.4b shows 3 curves produced by INDUS for different contact angles as well as a set of probabilities below that were used to generate the $\theta = 0^\circ$ curve. The model is plotted with the curves as dashed lines. I observe good qualitative agreement between the theory and the computed free energy. The locations of minima and maxima appear to match remarkably well, although the predicted barriers are almost twice as big. This discrepancy is probably a result of approximations used in deriving the free energy. The model assumes a flat interface rather than a curved interface, which is closer to the simulation than expected as shown in the four simulation snapshots in Figure 4.4a.

4.5 Infiltration Comparison

In order to determine how the free energy landscape influences infiltration, I simulate infiltration using different contact angles and observe the profiles of h vs t . Figure 4.5 shows curves from 4 different contact angles that are representative of different infiltration behaviors. For a contact angle above 84° , I observe that there is no infiltration happening within the simulation time; this is consistent with the discussion of critical contact angle θ_c in Chapter 3.6, which for flexible polymers under similar confinement ratios had a $\theta_c = 84^\circ$. However, below 84° infiltration is observed with two distinct modes. For higher contact angles, infiltration occurs periodically as a series of jumps from minimum to minimum in the free energy as denoted by the solid horizontal lines. These minima match the locations of constrictions along the axis of the capillary, which is consistent with the idea that the area of the free surface dominates the free energy. The residence time at each constriction is qualitatively observed to decrease as the contact angle increases, but there are insufficient data to recover a numerical residence time. Finally, for the lowest contact

angles ($\theta < 40^\circ$), infiltration progresses smoothly and without clear distinction of minima despite the presence of shallow wells in the free energy.

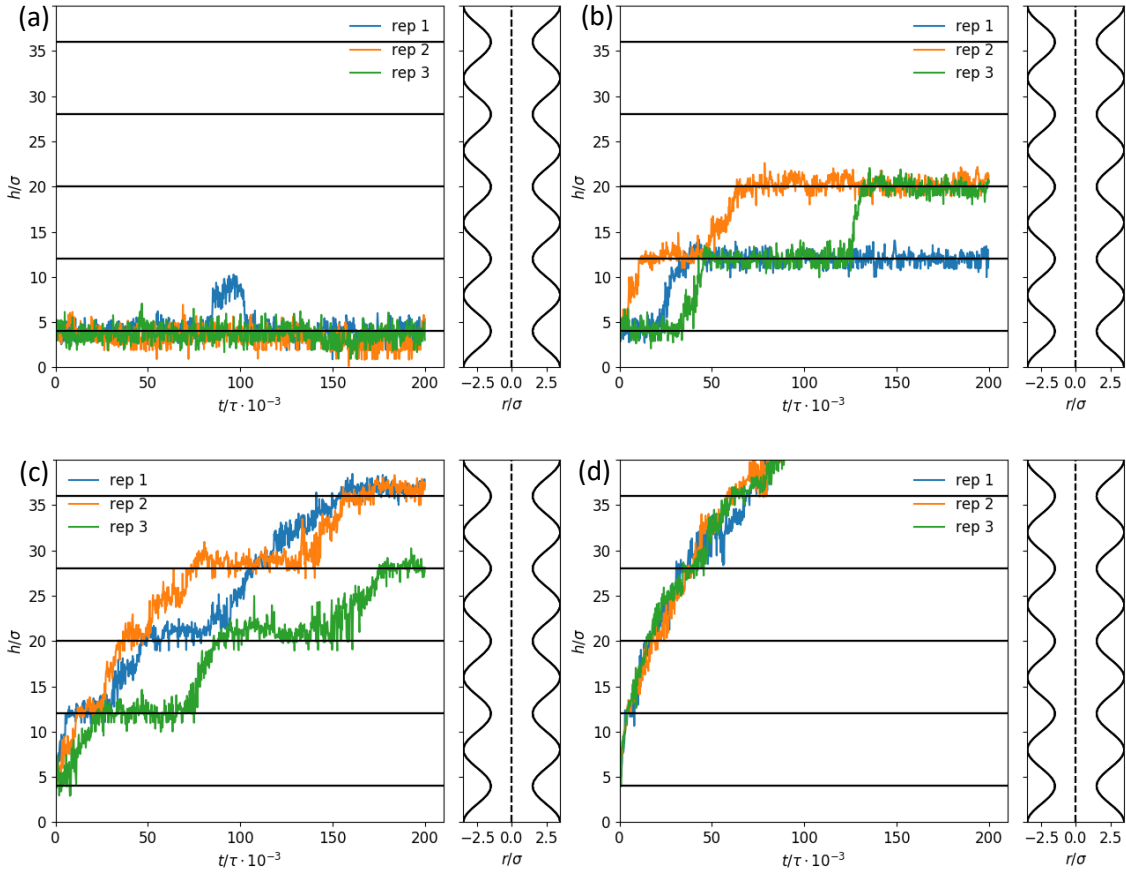


Figure 4.5: (a) At $\theta = 90^\circ$ infiltration is not observed at all. (b) At $\theta = 84^\circ$ infiltration is still observed, but proceeds stepwise jumping between minima, indicating that infiltration for this system is an activated process. (c) At $\theta = 72^\circ$ infiltration still proceeds stepwise, but individual jumps become harder to distinguish. (d) At $\theta = 40^\circ$ infiltration proceeds smoothly without jumping like would be expected in a Lucas-Wasburn system.

4.6 Summary

In conclusion, capillaries with non-constant cross-section have a rich and dynamic and free energy landscape that could provide insight into infiltration in nanoparticle packings. From continuum theory, I observed that the free energy of infiltration into a wavy capillary can exhibit barriers corresponding to voids along the axis of the capillary. From molecular dynamics simulations of polymer infiltration into wavy capillaries, I also observe that when the barriers are low enough, infiltration can still proceed, but appears to follow an activated pathway. This implies that rather than smoothly infiltrating along the capillary, the polymers are forced to jump from constriction to constriction following a probability related to the free energy barriers. These constrictions appear to act like enthalpic traps that polymers must overcome in order to penetrate deeper into the pore. It also implies that probability of making it over the barrier could be exponentially improved by increasing the temperature at which infiltration occurs.

CHAPTER 5: Conclusions and Outlook

5.1 Conclusions

Polymers infiltrating under extreme confinement exhibit a range of different behaviors not seen in bulk. These make it possible for polymer infiltration to be an excellent means to create polymer nanocomposites by using capillarity to infiltrate a nanoparticle film. Additionally, it can be used to create gradient and uniformly porous nanocomposite thin films by changing the relative thicknesses of the initial layers. These films have excellent mechanical properties and porosity even at very low polymer fill fractions due to reinforcement from particle bridging[20], making them excellent candidates for separation membranes and lightweight structural materials.

Infiltration of cylindrical capillaries and nanoparticle packings comes at the loss of polymer entropy. This is demonstrated by the depression in the critical contact angle, which is found to decrease for short chains and plateau for long chains. In melts, this is due to the melt entropy being constant for different chain lengths. However, stiffer chains experience a bigger loss of melt entropy, making it less energetically feasible for them to infiltrate. This ultimately means that they require stronger wetting in order to infiltrate under extreme confinement.

Finally, capillaries with sinusoidally varying diameters are potential model systems for understanding how variations in cross-section affect infiltration in nanoparticle packings. The free energy of these capillaries is observed to have local minima and maxima around constrictions and expansions, respectively. This is due to the large change in free surface area, which dominates the free energy. Barriers between these free

energy wells lead to different infiltration behaviors depending on the contact angle. Below 90° non-infiltration, activated jumping, and Lucas-Washburn like infiltration are observed. This indicates that there may be new and important ways to tune infiltration in nanoparticle packings that hadn't been considered previously.

From the findings of this study we can see that there are a number of outstanding questions that merit investigation. Studies on the confinement of stiff polymers and DNA molecules indicate that other regimes of confinement could yield surprising results compared to the de Gennes regime studied here for melts of flexible and semi-flexible polymers. It is not understood whether polymers would experience even greater resistance to infiltration at higher stiffnesses, or whether they could infiltrate via an entirely different mechanism. These regimes could also yield interesting results if the infiltration was performed in solvent instead of the melt state since the solvent quality would form an integral part of the infiltration mechanism. Finally, the free energy of infiltration could be greatly affected by the nature of the packings themselves and the anisotropy of the nanoparticles that make them up. We already know that polymers experience greater resistance to infiltration in capillaries with a high wave amplitude, but it is not known whether that translates into resistance in anisotropic packings.

We should also consider the temporal characteristics of polymer infiltration rather than just the free energy. The effect of confinement on polymer viscosity and infiltration rate has indicated that the chain dynamics can change drastically compared to bulk and are non-monotonic. This could provide many new questions for study, including whether we can observe polymer dead zones and disentanglement effects directly in MD

simulations. It could also be useful to examine whether the extensional viscosity and shear thinning characteristics of the polymers play a role in the mechanics of polymers with different chain lengths and stiffnesses. In the following sections I will discuss these questions in more detail and put forward some preliminary research that may indicate interesting avenues for the further research.

5.2 Confinement Free Energy of Stiff Polymers

For biopolymers and very stiff synthetic varieties, $D < l_p$, the de Gennes free energy breaks down. Instead of following random statistics, the polymers behave more like stiff rods that are deflected by the capillary walls. Depending on the type of polymer, the free energy can be described using a couple of different theories, although the two most well known were put forth by Odijk[64]–[66]. For many stiff polymers under strong confinement, the free energy is described in terms of a deflection length, $\lambda \approx (D^2 l_p)^{1/3}$ which represents the distance between points of contact between the polymer and the capillary as it is deflected along the capillary axis. I did not consider this case in my research as the polymers I modeled never had sufficiently high stiffness values to deflect along the length of the capillary.

More recently, there has been a push to unite the de Gennes and Odijk regimes into one theory. The most successful model to date is known as the Telegraph Model and describes polymers using a 1-D random walk[66]. It is unclear whether my polymers fall in this regime, but it may be informative to revisit some of the free energy arguments in

this paper with knowledge of the telegraph model to look at how bio-polymers and other stiff polymers infiltrate under such extreme confinement.

5.3 Free Energy landscape with solvent addition

While all the studies conducted in this thesis were performed on polymers in the melt state, infiltration can also occur in the presence of solvent. Solvent driven Infiltration of Polymers (SIP) is related to CaRI but relies on the entropy of mixing of polymers in solvent rather than capillary forces to induce infiltration[67]. Thus, by using different solvents with a range of solvent qualities for a particular polymer, it is possible to change both the rate and extent of infiltration into the nanoparticle packings.

Figure 5.1 shows a schematic demonstration of the SIP process. The process starts with a polymer nanoparticle bilayer, to which solvent vapor is introduced. Due to the small size of the nanoparticles which leads to high local curvature in the packing, the solvent vapor condenses within the top layer of the film. It then diffuses into the lower polymer layer and swells it, mobilizing polymers chains to infiltrate.

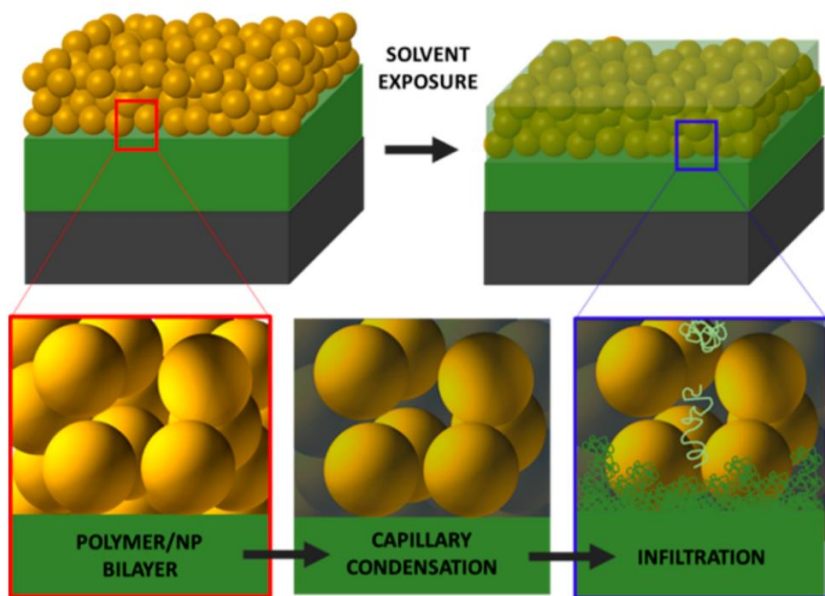


Figure 5.1: Schematic illustration of solvent-driven infiltration of polymer (SIP) into a NP film. A polymer/NP bilayer is annealed with solvent vapor, leading to capillary condensation of solvent in the NP packing, followed by swelling and infiltration of polymer[67].

From Figure 5.2a, it is observed that for a polystyrene (PS) and silica bi-layer, a smaller fraction of the nanoparticle film is infiltrated for higher Flory-Huggins χ parameter. This is because solvents with higher χ have weaker interactions with PS and therefore, are poorer solvents. Poorer solvents are not as good at swelling and softening the polymer layer, thus leading to less infiltration. It is also observed that the extent of infiltration is greater for packings made with smaller nanoparticles. Figure 5.2b shows that even very high molecular weight polymers can infiltrate into nanoparticle packings with good solvents.

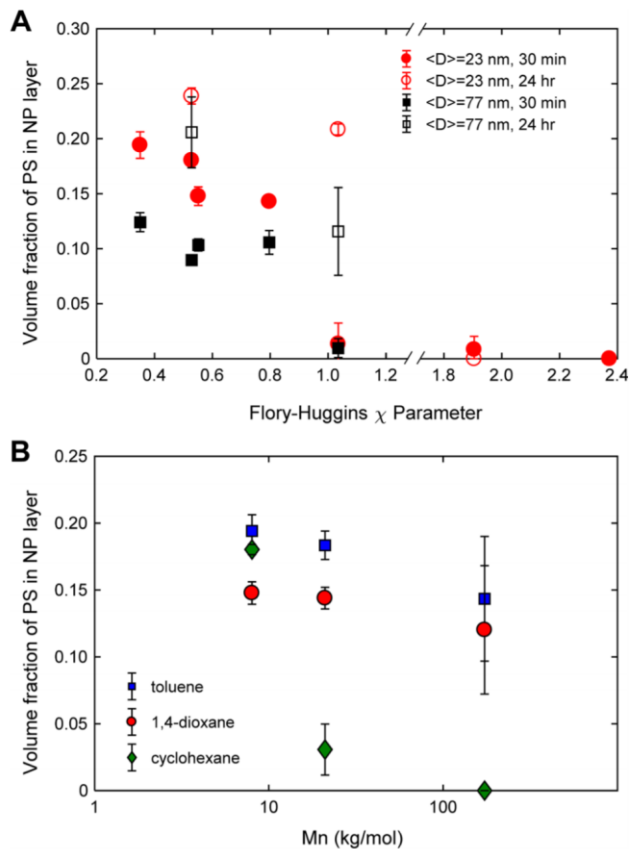


Figure 5.2: Volume fraction of PS in the NP packing (ϕ_{PS}) (A) for PS ($M_n = 8000$ g/mol) into 23 nm particle packings (circles) and 77 nm particle packings (diamonds), after 30 min (closed) or 24 h (open) of vapor exposure for various solvents at different χ , and (B) using different good solvents ($\chi < \chi_c$) as a function of PS molecular weight after 30 min of vapor exposure[67].

SIP has the advantage over CaRI of not requiring heat to mobilize the polymer. Also, the wide range of polymer and solvent interactions available provide a way to finely tune the extent of infiltration. However, free energy of infiltration in the presence of solvent is not well understood. It is possible, since SIP does not rely on capillarity that the critical contact angle for infiltration would match the Lucas-Washburn limit or that cross-sectional variation has a different impact on the infiltration process. These would be

interesting questions to determine since SIP is a promising route toward improving the environmental footprint of CaRI.

5.4 Free energy of infiltration in packings of anisotropic particles

The packings and capillaries in this study assume roughly spherical particles. However, packings of platelets or rods with high aspect ratio could have very different free energy landscapes due to their different packing fractions, cross-sectional variation and morphologies. An example of nanoparticle anisotropy influencing polymer behavior can be observed in studies of polymers diffusing within nanocomposites. These studies indicate that high aspect ratio nanoparticles can significantly and non-monotonically change the diffusivity of polymers[68], [69]. This is demonstrated in Figure 5.3 where panel (a) shows that polymer diffusivity decreases as a function of nanorod fraction when the polymers are shorter than the nanorod length. However, when polymers have a larger R_g than the nanorod length as shown in panel (b), the diffusivity initially drops but then recovers. This is attributed to an enhancement in polymer diffusivity along the axis of the nanorods, which is enhanced above the percolation threshold of the nanoparticles. This provide an interesting route towards creating structures that closely resemble the brick and mortar structures of nacre, or the Bouligand structures in the mantis shrimp dactyl club.

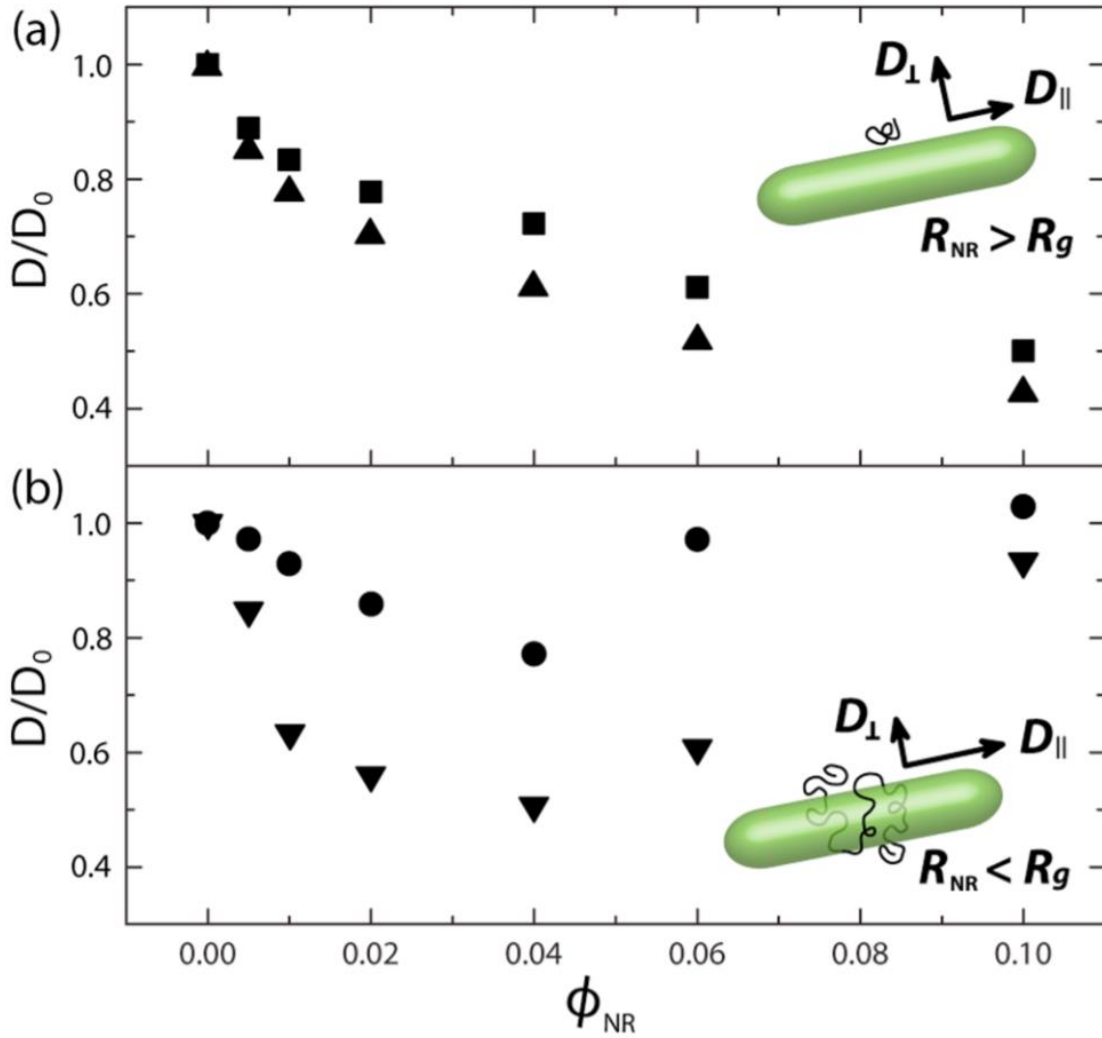


Figure 5.3: Reduced tracer diffusion coefficients of dPS for (a) $M_n = 168$ (squares) and 532 (triangles) kg mol^{-1} or (b) $M_n = 1866$ (circles) and 3400 (inverse triangles) kg mol^{-1} in nanocomposites containing NR-long ($\phi_{NR} = 0-0.1$) exhibiting a monotonic decrease or a minimum of diffusion coefficients, respectively. Insets describe the local polymer diffusion in the direction parallel (D_{\parallel}) and perpendicular (D_{\perp}) to NRs, depending on the relative size of the R_{NR} to R_g ; (a) isotropic tracer diffusion ($D_{\parallel} \cong D_{\perp}$) when $R_{NR} > R_g$ and (b) anisotropic tracer diffusion ($D_{\parallel} > D_{\perp}$) when $R_{NR} < R_g$ [69].

5.5 Influence of dynamics and extensional viscosity

Experimental studies of confined polymers undergoing CaRI in nanoparticle packings indicate that the viscosity increases several orders of magnitude relative to bulk for short chains[40], [48]. Figure 5.4 shows the relative viscosity increase and glass transition temperature increase with increasing confinement ratio.

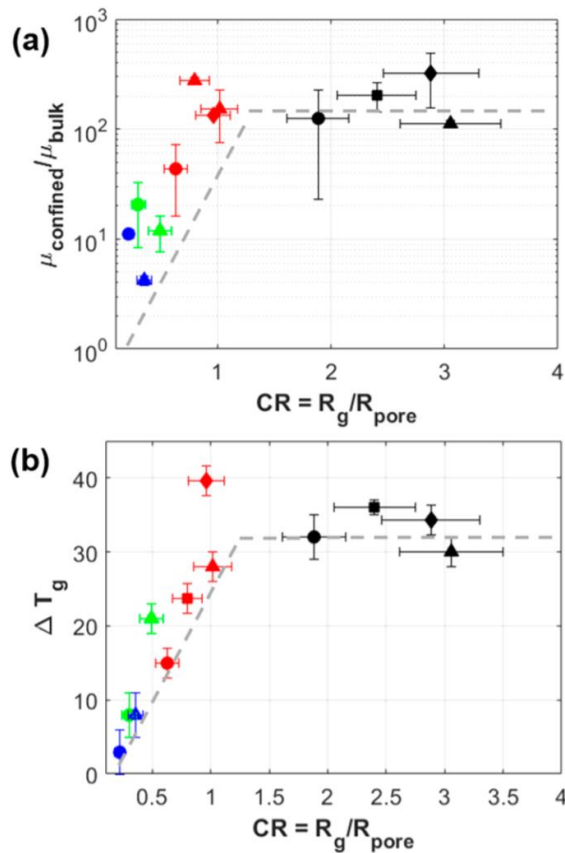


Figure 5.4: (a) Normalized viscosity ($\mu_{\text{confined}}/\mu_{\text{bulk}}$) obtained for PS undergoing CaRI at $T = 403$ K and the (b) ΔT_g ($T_g - T_{g,\text{bulk}}$) as a function of confinement ratio (CR). The lines are to guide the eye[21], [40].

However, this phenomenon is not easy to explain. The data from CaRI and glass transition temperature measurements indicate that both local and global chain dynamics

are slowing down, but the exact origin of this slow down remains a mystery. Theory indicates that viscosity should increase for short chains, and then drop for longer chains, however, the data agrees with the model qualitatively at best[48] as shown in Figure 5.5. This theory is based on the competition of two effects, the formation of a dead zone near the wall of the pore due to polymer absorption which increases the effective viscosity, and the loss of entanglements relative to the bulk for long chains leading to an overall decrease in viscosity.

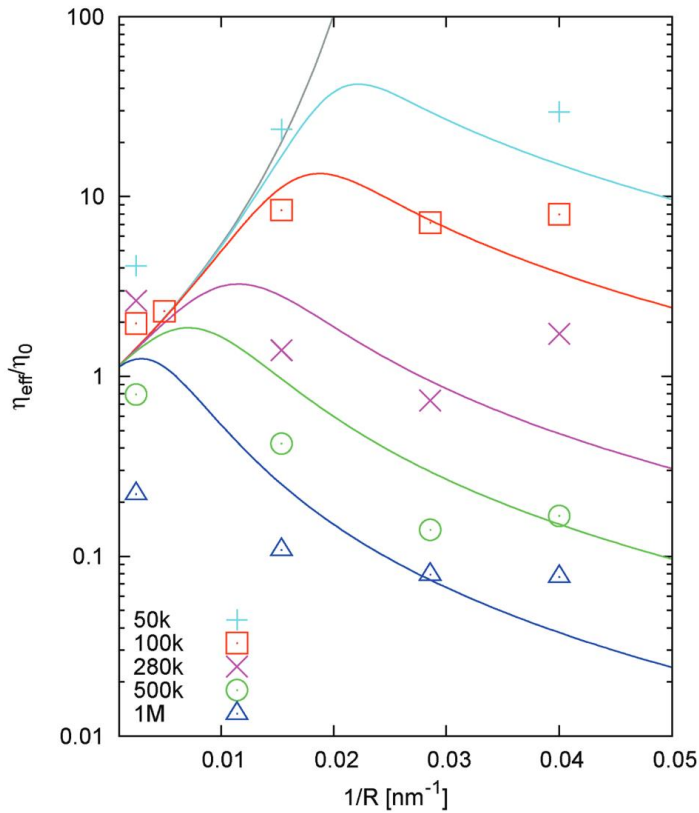


Figure 5.5: Comparison between the experiment and the theory. The symbols are shown for the experimental data taken from reference [14]. The lines are from theoretical prediction of Equation (25). [48]

Given the variation in cross-section, I suspect that the extensional viscosity of polymers will be important to the infiltration process. It would be interesting to determine whether extensional viscosity results in the increase in viscosity for short chain polymers. Additionally, determining the extensional viscosity in polymer flows through converging and diverging capillaries could provide a novel way to measure these properties in simulations of confinement rather than relying on bulk measurements.

BIBLIOGRAPHY

- [1] S. K. Kumar, V. Ganesan, and R. A. Riggleman, “Perspective: Outstanding theoretical questions in polymer-nanoparticle hybrids,” *J. Chem. Phys.*, vol. 147, no. 2, 2017.
- [2] Q. Li, K. Han, M. R. Gadinski, G. Zhang, and Q. Wang, “High Energy and Power Density Capacitors from Solution-Processed Ternary Ferroelectric Polymer Nanocomposites,” *Adv. Mater.*, vol. 26, no. 36, pp. 6244–6249, Sep. 2014.
- [3] T. C. Merkel *et al.*, “Ultrapерmeable, Reverse-Selective Nanocomposite Membranes,” *Science (80-.)*, vol. 296, no. 5567, pp. 519–522, 2002.
- [4] Y.-R. Huang *et al.*, “Polymer nanocomposite films with extremely high nanoparticle loadings via capillary rise infiltration (CaRI),” *Nanoscale*, vol. 7, no. 2, pp. 798–805, 2015.
- [5] F. Bouville, E. Maire, S. Meille, B. Van de Moortèle, A. J. A. J. Stevenson, and S. Deville, “Strong, tough and stiff bioinspired ceramics from brittle constituents.,” *Nat. Mater.*, vol. 13, no. 5, pp. 508–14, 2014.
- [6] U. G. K. Wegst, H. Bai, E. Saiz, A. P. Tomsia, and R. O. Ritchie, “Bioinspired structural materials,” *Nat. Mater.*, vol. 14, no. 1, pp. 23–36, 2015.
- [7] S. E. Naleway, J. R. A. Taylor, M. M. Porter, M. A. Meyers, and J. McKittrick, “Structure and mechanical properties of selected protective systems in marine organisms,” *Mater. Sci. Eng. C*, vol. 59, pp. 1143–1167, 2016.

- [8] F. Barthelat and R. Rabiei, "Toughness amplification in natural composites," *J. Mech. Phys. Solids*, vol. 59, no. 4, pp. 829–840, 2011.
- [9] N. A. Yaraghi and D. Kisailus, "Biomimetic Structural Materials: Inspiration from Design and Assembly," *Annu. Rev. Phys. Chem.*, vol. 69, no. 1, 2017.
- [10] K. S. Katti, D. R. Katti, S. M. Pradhan, and A. Bhosle, "Platelet interlocks are the key to toughness and strength in nacre," *J. Mater. Res.*, vol. 20, no. 05, pp. 1097–1100, 2005.
- [11] K. S. Katti and D. R. Katti, "Why is nacre so tough and strong?," *Mater. Sci. Eng. C*, vol. 26, no. 8, pp. 1317–1324, 2006.
- [12] L. M. Robeson, "The upper bound revisited," *J. Memb. Sci.*, vol. 320, no. 1–2, pp. 390–400, 2008.
- [13] Y. Chen, M. Jia, H. Xu, Y. Cao, and H. Fan, "Counterintuitive Gas Transport through Polymeric Nanocomposite Membrane: Insights from Molecular Dynamics Simulations," *J. Phys. Chem. C*, vol. 118, no. 48, pp. 28179–28188, 2014.
- [14] R. M. Barrer, J. A. Barrie, and M. G. Rogers, "Heterogeneous membranes: Diffusion in filled rubber," *J. Polym. Sci. Part A Gen. Pap.*, vol. 1, no. 8, pp. 2565–2586, 1963.
- [15] W. Caseri, "Nanocomposites of polymers and metals or semiconductors: Historical background and optical properties," *Macromol. Rapid Commun.*, vol. 21, no. 11, pp. 705–722, 2000.

- [16] S. Srivastava and N. A. Kotov, "ChemInform Abstract: Composite Layer-by-Layer (LBL) Assembly with Inorganic Nanoparticles and Nanowires," *ChemInform*, vol. 40, no. 14, pp. 1831–1841, 2009.
- [17] J. B. Schlenoff and G. Decher, Eds., *Multilayer Thin Films: Sequential Assembly of Nanocomposite Materials*, 2nd ed. Wiley-VCH, Weinham, 2012.
- [18] C. Lu, Z. Cui, Y. Wang, Z. Li, C. Guan, and B. Yang, "Preparation and characterization of ZnS – polymer nanocomposite films with high refractive index," pp. 2189–2195, 2003.
- [19] A. Shavit and R. a Riggleman, "The dynamics of unentangled polymers during capillary rise infiltration into a nanoparticle packing.," *Soft Matter*, vol. 11, no. 42, pp. 8285–95, 2015.
- [20] J. L. Hor, Y. Jiang, D. J. Ring, R. A. Riggleman, K. T. Turner, and D. Lee, "Nanoporous Polymer-Infiltrated Nanoparticle Films with Uniform or Graded Porosity via Undersaturated Capillary Rise Infiltration," *ACS Nano*, vol. 11, no. 3, pp. 3229–3236, 2017.
- [21] J. L. Hor, H. Wang, Z. Fakhraai, and D. Lee, "Effects of polymer-nanoparticle interactions on the viscosity of unentangled polymers under extreme nanoconfinement during capillary rise infiltration," *Soft Matter*, 2018.
- [22] Y. Yao *et al.*, "Capillary Imbibition, Crystallization, and Local Dynamics of Hyperbranched Poly(ethylene oxide) Confined to Nanoporous Alumina,"

- Macromolecules*, vol. 50, no. 21, pp. 8755–8764, 2017.
- [23] S. Alexandris, P. Papadopoulos, G. Sakellariou, M. Steinhart, H. J. Butt, and G. Floudas, “Interfacial energy and glass temperature of polymers confined to nanoporous alumina,” *Macromolecules*, vol. 49, no. 19, pp. 7400–7414, 2016.
- [24] S. Alexandris, G. Sakellariou, M. Steinhart, and G. Floudas, “Dynamics of unentangled cis -1,4-polyisoprene confined to nanoporous alumina,” *Macromolecules*, vol. 47, no. 12, pp. 3895–3900, 2014.
- [25] M. Zhang, P. Dobriyal, J. T. Chen, T. P. Russell, J. Olmo, and A. Merry, “Wetting transition in cylindrical alumina nanopores with polymer melts,” *Nano Lett.*, vol. 6, no. 5, pp. 1075–1079, 2006.
- [26] D. I. Dimitrov, A. Milchev, and K. Binder, “Capillary rise in Nanopores: Molecular dynamics evidence for the Lucas-Washburn equation,” *Phys. Rev. Lett.*, vol. 99, no. 5, pp. 1–4, 2007.
- [27] D. I. Dimitrov, A. Milchev, and K. Binder, “Forced imbibition—a tool for separate determination of Laplace pressure and drag force in capillary filling experiments,” *Phys. Chem. Chem. Phys.*, vol. 10, no. 14, p. 1867, 2008.
- [28] E. W. Washburn, “The dynamics of capillary flow,” *Phys. Rev.*, vol. 17, no. 3, pp. 273–283, 1921.
- [29] P. Huber, “Soft matter in hard confinement: phase transition thermodynamics, structure, texture, diffusion and flow in nanoporous media,” *J. Phys. Condens.*

Matter, vol. 27, no. 10, p. 103102, Mar. 2015.

- [30] S. Gruener, H. E. Hermes, B. Schillinger, S. U. Egelhaaf, and P. Huber, “Capillary rise dynamics of liquid hydrocarbons in mesoporous silica as explored by gravimetry, optical and neutron imaging: Nano-rheology and determination of pore size distributions from the shape of imbibition fronts,” *Colloids Surfaces A Physicochem. Eng. Asp.*, vol. 496, pp. 13–27, 2016.
- [31] N. Fries and M. Dreyer, “The transition from inertial to viscous flow in capillary rise,” *J. Colloid Interface Sci.*, vol. 327, no. 1, pp. 125–128, 2008.
- [32] N. Ichikawa and Y. Satoda, “Interface Dynamics of Capillary Flow in a Tube under Negligible Gravity Condition,” *J. Colloid Interface Sci.*, vol. 162, no. 2, pp. 350–355, Feb. 1994.
- [33] S. Gruener and P. Huber, “Imbibition in mesoporous silica: Rheological concepts and experiments on water and a liquid crystal,” *J. Phys. Condens. Matter*, vol. 23, no. 18, 2011.
- [34] W. W. Liou, Y. Peng, and P. E. Parker, “Analytical modeling of capillary flow in tubes of nonuniform cross section,” *J. Colloid Interface Sci.*, vol. 333, no. 1, pp. 389–399, May 2009.
- [35] H. Czachor, “Modelling the effect of pore structure and wetting angles on capillary rise in soils having different wettabilities,” *J. Hydrol.*, vol. 328, no. 3–4, pp. 604–613, 2006.

- [36] A. Borhan and K. K. Rungta, "Lucas-Washburn kinetics for capillary penetration between periodically corrugated plates," *Journal of Colloid And Interface Science*, vol. 155, no. 2. pp. 438–443, 1993.
- [37] R. Sharma and D. S. Ross, "Kinetics of liquid penetration into periodically constricted capillaries," *J. Chem. Soc. Faraday Trans.*, vol. 87, no. 4, p. 619, 1991.
- [38] M. Rubinstein and R. H. Colby, *Polymer physics*. 2003.
- [39] F. Brochard and P. G. de Gennes, "Conformations de polymères fondus dans des pores très petits," *J. Phys. Lettres*, vol. 40, no. 16, pp. 399–401, 1979.
- [40] J. L. Hor, H. Wang, Z. Fakhraai, and D. Lee, "Effect of Physical Nanoconfinement on the Viscosity of Unentangled Polymers during Capillary Rise Infiltration," *Macromolecules*, vol. 51, no. 14, pp. 5069–5078, 2018.
- [41] W. Bin Young, "Analysis of capillary flows in non-uniform cross-sectional capillaries," *Colloids Surfaces A Physicochem. Eng. Asp.*, vol. 234, no. 1–3, pp. 123–128, 2004.
- [42] R. Auhl, R. Everaers, G. S. Grest, K. Kremer, and S. J. Plimpton, "Equilibration of long chain polymer melts in computer simulations," *J. Chem. Phys.*, vol. 119, no. 24, pp. 12718–12728, 2003.
- [43] K. Kremer and G. S. Grest, "Dynamics of entangled linear polymer melts: A molecular-dynamics simulation," *J. Chem. Phys.*, vol. 92, no. 8, pp. 5057–5086, Apr. 1990.

- [44] J. Martín and C. Mijangos, “Tailored polymer-based nanofibers and nanotubes by means of different infiltration methods into alumina nanopores,” *Langmuir*, vol. 25, no. 2, pp. 1181–1187, 2009.
- [45] W. S. Tung, R. J. Composto, R. A. Riggleman, and K. I. Winey, “Local polymer dynamics and diffusion in cylindrical nanoconfinement,” *Macromolecules*, vol. 48, no. 7, pp. 2324–2332, 2015.
- [46] H. Xiang, K. Shin, T. Kim, S. I. Moon, T. J. McCarthy, and T. P. Russell, “Block copolymers under cylindrical confinement,” *Macromolecules*, vol. 37, no. 15, pp. 5660–5664, 2004.
- [47] N.-K. Lee *et al.*, “Non-ideality of polymer melts confined to nanotubes,” *EPL*, vol. 93, no. 4, p. 48002, Feb. 2011.
- [48] Y. Yao, H.-J. Butt, G. Floudas, J. Zhou, and M. Doi, “Theory on Capillary Filling of Polymer Melts in Nanopores,” *Macromol. Rapid Commun.*, vol. 39, no. 14, p. 1800087, 2018.
- [49] K. Kremer and G. S. Grest, “Dynamics of entangled linear polymer melts: A molecular-dynamics simulation,” *J. Chem. Phys.*, vol. 92, no. 8, pp. 5057–5086, 1990.
- [50] R. Kumar, M. Goswami, B. G. Sumpter, V. N. Novikov, and A. P. Sokolov, “Effects of backbone rigidity on the local structure and dynamics in polymer melts and glasses,” *Phys. Chem. Chem. Phys.*, vol. 15, no. 13, p. 4604, 2013.

- [51] J. Rafiee *et al.*, “Wetting transparency of graphene,” *Nat. Mater.*, vol. 11, no. 3, pp. 217–222, Mar. 2012.
- [52] J. Alejandro, D. J. Tildesley, and G. A. Chapela, “Molecular dynamics simulation of the orthobaric densities and surface tension of water,” *J. Chem. Phys.*, vol. 102, no. 11, pp. 4574–4583, 1995.
- [53] D. G. Legrand and G. L. Gaines, “Surface tension of homologous series of liquids,” *J. Colloid Interface Sci.*, vol. 42, no. 1, pp. 181–184, 1973.
- [54] D. T. Wu, G. H. Fredrickson, J. -P Carton, A. Ajdari, and L. Leibler, “Distribution of chain ends at the surface of a polymer melt: Compensation effects and surface tension,” *J. Polym. Sci. Part B Polym. Phys.*, vol. 33, no. 17, pp. 2373–2389, 1995.
- [55] M. W. Matsen and P. Mahmoudi, “Segregation of chain ends to the surface of a polymer melt,” *Eur. Phys. J. E*, vol. 37, no. 8, p. 78, Aug. 2014.
- [56] R. J. Lang, W. L. Merling, and D. S. Simmons, “Combined Dependence of Nanoconfined T_g on Interfacial Energy and Softness of Confinement,” *ACS Macro Lett.*, vol. 3, no. 8, pp. 758–762, Aug. 2014.
- [57] J. N. Israelachvili, *Intermolecular and Surface Forces: Third Edition*. 2011.
- [58] A. J. Patel, P. Varilly, D. Chandler, and S. Garde, “Quantifying Density Fluctuations in Volumes of All Shapes and Sizes Using Indirect Umbrella Sampling,” *J. Stat. Phys.*, vol. 145, no. 2, pp. 265–275, 2011.
- [59] S. Prakash, E. Xi, and A. J. Patel, “Spontaneous Recovery of Superhydrophobicity

on Nanotextured Surfaces,” pp. 1–12, 2015.

- [60] H. Jiang, S. Fialoke, Z. Vicars, and A. J. Patel, “Characterizing surface wetting and interfacial properties using enhanced sampling (SWIPES),” *Soft Matter*, vol. 15, no. 5, pp. 860–869, 2019.
- [61] B. Roux, “The calculation of the potential of mean force using computer simulations,” *Comput. Phys. Commun.*, vol. 91, no. 1–3, pp. 275–282, 1995.
- [62] F. Zhu and G. Hummer, “Convergence and error estimation in free energy calculations using the weighted histogram analysis method,” *J. Comput. Chem.*, vol. 33, no. 4, pp. 453–465, 2012.
- [63] J. S. Hub, B. L. De Groot, and D. Van Der Spoel, “g_whamsA Free Weighted Histogram Analysis Implementation Including Robust Error and Autocorrelation Estimates,” pp. 3713–3720, 2010.
- [64] T. Odijk, “The statistics and dynamics of confined or entangled stiff polymers,” *Macromolecules*, vol. 16, no. 8, pp. 1340–1344, Aug. 1983.
- [65] T. Odijk, “Theory of lyotropic polymer liquid crystals,” *Macromolecules*, vol. 19, no. 9, pp. 2313–2329, Sep. 1986.
- [66] E. Werner, G. K. Cheong, D. Gupta, K. D. Dorfman, and B. Mehlig, “One-Parameter Scaling Theory for DNA Extension in a Nanochannel,” *Phys. Rev. Lett.*, vol. 119, no. 26, pp. 1–6, 2017.
- [67] N. Manohar, K. J. Stebe, and D. Lee, “Solvent-Driven Infiltration of Polymer

(SIP) into Nanoparticle Packings,” *ACS Macro Lett.*, vol. 6, no. 10, pp. 1104–1108, 2017.

[68] M. Mu, N. Clarke, R. J. Composto, and K. I. Winey, “Polymer diffusion exhibits a minimum with increasing single-walled carbon nanotube concentration,” *Macromolecules*, vol. 42, no. 18, pp. 7091–7097, 2009.

[69] J. Choi, N. Clarke, K. I. Winey, and R. J. Composto, “Fast polymer diffusion through nanocomposites with anisotropic particles,” *ACS Macro Lett.*, vol. 3, no. 9, pp. 886–891, 2014.